Chapter 7

Single-Ion Channel

This chapter describes our BD simulations of a model catenary channel based on the hour-glass shaped acetylcholine receptor channel [70].

7.1 Model

7.1.1 Shape of the Channel

A catenary channel was generated by rotating the closed curve shown in Fig. 7.1 around the symmetry, z-axis. The vestibule of the channel, whose shape is similar to that visible in the electron microscope picture of the acetylcholine channel [70], was generated by a hyperbolic cosine function, $y = a \cosh x/a$, where $a = 4.87$ Å. The radius of the entrance of the vestibule was fixed at 13 Å. Two identical vestibules were connected with a cylindrical transmembrane region of length 10 Å and radius 4 Å. The total interior volume of the model channel was 2.16×10^{-26} m^3. We assumed, for simplicity, that the two vestibules are identical in size, although the image of the channel produced by Toyoshima and Unwin [70] shows that the extracellular vestibule is larger than the intracellular vestibule.

7.1.2 Dipoles in the Protein Wall

To investigate how the permeation of ions across the channel is influenced by the presence and absence of dipoles in the protein wall, we placed in some simulations a set of 4 dipoles inside the protein boundary at $z = 5$ Å and another set of 4 dipoles at $z = -5$ Å. Their orientations were perpendicular to the central axis of the lumen (z-axis). For each dipole, the negative pole, placed 2 Å inside the water-protein boundary, was separated from the positive pole by 5 Å. Thus, if 5/16 of an elementary charge was placed on each pole, then the total moments of 4 such dipoles would be 100×10^{-30} Coulomb-meter. The same configuration of dipoles was used in all the simulations, giving rise to an attractive potential for sodium ions and

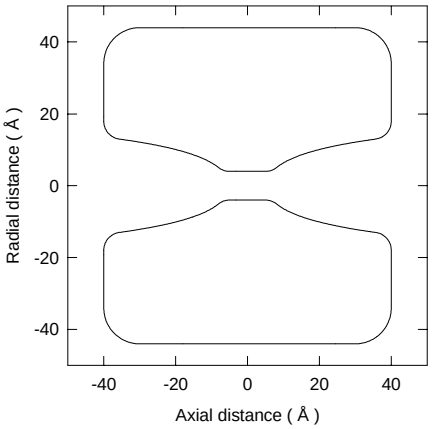

Figure 7.1: Idealized biological ion channel. A model channel with two catenary vestibules was generated by rotating the closed curves along the symmetry z-axis by 180^o. To approximate the shape of the acetylcholine receptor channel, vestibules at each side of the membrane were constructed using a hyperbolic cosine function, $y = a \cosh\ x/a$ where $a = 4.87$ Å. The radius of the entrance of the vestibule was fixed at 13 Å and the cylindrical transmembrane segment had a radius of 4 Å. Each cylindrical reservoir, 60 Å in diameter and 22 Å in height, contained a fixed number of sodium and chloride ions. Unless stated otherwise, the ionic concentration in the volume composed of the channel vestibules and the reservoirs was 300 mM. The cylindrical reservoir had a glass boundary, in that an ion moving out of the boundary was reflected back into the reservoir.

a repulsive potential for chloride ions in the channel. These fixed charges represent the charged side chains thought to form a ring around the entrance of the constricted region [71], and their nearby counter charges. For convenience, we adjust the amount of charge rather than the number or positions of the charges, but in reality the side chains of charged amino acid residues would have one electron charge each if they are fully ionized or unprotonated at neutral pH. Polar groups located in the transmembrane segment of the channel that may rotate in and out to form temporary hydrogen bonds with an ion navigating across it, as found in gramicidin A pores, are not explicitly modeled in our single ion channel.

7.1.3 Energy Barrier in the Transmembrane Segment

An ion in the vestibule needs to surmount an energy barrier to traverse the narrow, constricted segment of the channel. The presence of such an additional energy barrier in the gramicidin pore has been revealed by molecular dynamics calculations. Intuitively, this barrier arises from the interactions between the protein wall and the hydrated ion as the ion negotiates its way into the narrow, cylindrical, transmembrane pore. To enter the narrow segment, the hydration shell of an ion needs to be re-arranged or some of the water molecules in the primary or secondary hydration shell need to be substituted with polar groups on the protein wall. To re-arrange the ion-water geometry requires an additional energy, and the ion can surmount such a barrier only when it gains a sufficient kinetic energy. To mimic a barrier present in the ion channel, we placed in some simulations a potential step near the constricted segment of the channel. The energy must be paid to enter the neck, and is returned when the ion exits. The method we used for implementing such a potential barrier in the Brownian dynamics algorithm is detailed below.

7.1.4 Applied Electric Field

A potential difference across a lipid membrane is produced by a surface charge density on each side of the membrane. In microscopic terms, the surface charge density is a cloud of unpaired ions on either side of the membrane. Because these clouds are too diffuse to be explicitly included in our simulation, we apply an external electric field E of a constant strength to represent the average effect of the ionic clouds. In the absence of any dielectric boundary, the potential difference across a channel with the length d is E/d. The presence of a dielectric boundary, however, severely distorts the field, enhancing it in the transmembrane segment and attenuating it in the vestibule. Thus, the precise potential difference will depend on the selected reference points at the two sides of the catenary channel. For simplicity, we apply a field strength of 10^7 V m^{-1} and refer to it as an applied potential

of 100 mV.

7.2 Theory

7.2.1 Pöschl-Teller Function

If the ionic concentrations on the two faces of the channel are the same, the current-voltage relationship obtained from patch-clamp recordings is in general ohmic. The current-voltage relationship deduced from our simulations becomes nonlinear whenever there is a potential barrier for the ions to surmount in order to cross the channel (Fig. 7.8). This deviation from Ohm's law is more pronounced when the potential barrier is large. Although the precise shape of the curve cannot be deduced *a priori*, it is easy to see how such a curvature in the current-voltage relationship would arise. The presence of a barrier is less of an impediment when the driving force is large. This intuitive observation suggests a modification of Ohm's law with the Pöschl-Teller function

$$I = \frac{\gamma V}{1 + \beta/\cosh(eV/V_B)}, \tag{7.1}$$

where γ is the conductance, V_B is the barrier height, and β is a dimensionless constant. When $eV \gg V_B$, the denominator goes to 1, and one recovers Ohm's law. For $eV \ll V_B$, Eq. (7.1) is again linear but with a conductance reduced to $\gamma V/(1+\beta)$. The nonlinearities in the $I-V$ curves become apparent only when $eV > V_B$, which corresponds to the region $V \approx 100 \sim 200$ mV for our model channel.

7.2.2 Michaelis-Menten Equation

Experimentally it has been shown that the current first increases with an increasing ionic concentration and then saturates [59, 31]. Such a relationship is expected to be found when the transport of ions across the channel is determined by two independent processes, one of which depends upon ion concentration and one that does not. In our simulations, for example, the time τ_1 it takes for an ion to arrive near the constricted segment is inversely proportional to the electric field E and ionic concentration $[c]$, whereas the time τ_2 it takes for the ion to acquire a sufficient kinetic energy to surmount the barrier placed near the transmembrane segment and traverse the second half of the channel is relatively independent of the ionic concentration but dependent only on the electric field. Thus, assuming a uniform electric field, the transit times can be written as

$$\tau_1 = \frac{k_1}{[c]\ E}, \quad \tau_2 = \frac{k_2}{E}, \tag{7.2}$$

where k_1 and k_2 are constants. The total time τ it takes an ion to traverse the channel is $\tau = \tau_1 + \tau_2$, and the current flowing across it will be $I = nze$, where the number n of ions carrying charges ze is $1/\tau$. Thus, the current is inversely proportional to the total transit time, that is,

$$I \propto \frac{ze}{(\tau_1 + \tau_2)} = \frac{zeE}{k_1/[c] + k_2}. \tag{7.3}$$

For large concentrations, Eq. (7.3) approaches to a maximum value that we denote by $I_{\max} = zeE/k_2$. Factoring out k_2 and introducing $K_s = k_1/k_2$, Eq. (7.3) can be written in the form

$$I = \frac{I_{\max}}{1 + K_s/[c]}. \tag{7.4}$$

The form of this equation is identical to that of the Michaelis-Menten equation, which is derived under an entirely different set of assumptions. The curves calculated from Eq. (7.4) fit the current-concentration relationships obtained from our simulations reasonably well (see Fig. 7.9).

7.3 Methods

7.3.1 Stochastic Boundaries

To ensure that the desired intracellular and extracellular ion concentrations were maintained throughout the simulation, a stochastic boundary was applied. When an ion crossed the transmembrane segment, an ion of the same species was transplanted so as to maintain the original concentrations on both sides of the membrane. For example, if a sodium ion from the left-hand side of the channel crossed the narrow transmembrane segment and reached the imaginary plane at $z = 10$ Å, then a sodium ion located at the furthermost right-hand reservoir was taken out and placed in the far left-hand side of the left reservoir. When transplanting ions, we chose a point no closer to another ion than the defined safe distance. The stochastic boundary trigger points, located at $z = \pm 10$ Å, were checked at each time step of the simulation.

7.3.2 Short Timestep Algorithm

The use of a long time step causes a problem in implementing potential barriers and steps in Brownian dynamics as short range forces. In our simulations, the Brownian dynamics algorithm operates predominantly in the diffusive regime. In other words, random forces are far more important than the velocity on the previous step in determining an ion's new velocity and position. The algorithm devised by van Gunsteren and Berendsen [72] uses

the factors $[\exp(-\gamma\Delta t)]$ and $[1-\exp(-\gamma\Delta t)]$ to switch between kinetic and diffusive regions. With the long time step ($\Delta t = 100$ fs) that we use,

$$\begin{aligned} 1-\exp(-\gamma_{\mathrm{Na}}\Delta t) &= 0.9997, \\ 1-\exp(-\gamma_{\mathrm{Cl}}\Delta t) &= 0.9666. \end{aligned}$$

Thus, for chloride ions only 3% of the previous velocity remains after one time step, while the motion of sodium ions is in effect purely diffusive, with no velocity correlation between steps. Since an ion can move a large fraction of the barrier width in a single time step (around 0.3 Å on average), the effect of the barrier force on the ion's motion will not be accurately integrated. Also, in the diffusive regime, external forces cause only an average drift velocity which does not move the ion far in a single time step. For example, a repulsive force of 120×10^{-12} N ($3\ kT_r$ over 1 Å) produces a drift velocity of 39 ms^{-1} for sodium, and a displacement of 0.04 Å in one time step. This is only 1/7 of the average random displacement in one time step—an ion can diffuse right through a potential barrier before the barrier force has time to act.

To obviate these problems, we used two different time steps: a short time step of 1 fs when an ion was in the process of climbing or descending the barrier and the long time step of 100 fs otherwise. A smooth potential barrier of height V_B was erected at $z = \pm 10$ Å (5 Å from the entrance of the cylindrical segment), with the profiles at the ends as

$$U(s) = V_B(10s^3 - 15s^4 + 6s^5), \tag{7.5}$$

where

$$s = \frac{z - z_b}{\Delta z} + \frac{1}{2}. \tag{7.6}$$

Here $z_b = \pm 10$ Å is the location of the center of the profile and $\Delta z = 1$ Å is the width of the profile. The potential profile $U(s)$ is chosen such that it rises from zero at $z = \pm 10.5$ to V_B at $z = \pm 9.5$, and the first and second derivatives of $U(s)$ vanish at $z = \pm 9.5$ and $z = \pm 10.5$. The force due to the barrier is obtained by differentiating Eq. (7.5).

We included a safety distance of 0.5 Å in the potential profile. Thus, whenever ions were in the band of $z = 9$ - 11 Å or $z = -9$ to -11 Å, we switched from long time steps to an equivalent sequence of short time steps for those ions. Trajectories of ions in these bands were determined by a sequence of 100 short time steps for the subsequent 100 fs. In the meantime, all the other ions were simulated for a single long time steps in the normal way. The long range (electrostatic) forces on the ion were calculated at the start of the sequence of 100 short steps, and held constant thereafter. Similarly, reflection from the boundary walls was done once at the end of the sequence of short steps. The force from the barrier, however, was recalculated for each short step, thus ensuring that the effect of the barrier on the ion's motion would be accurately simulated.

7.3.3 Procedure for Calculating Conductance

Simulations under various conditions, each lasting between 500,000 and 2,000,000 time steps, were repeated many times, from 5 to 9 trials. For the first trial, the positions of ions in the reservoirs were assigned randomly with the proviso that the minimum ion-ion distance should be 2.7 Å, or 1.5 times the radius of a chloride ion. For successive trials, the positions of the ions in the last time step were used as the initial starting positions of the following trial. The current given in pA was extrapolated from the total number of ions traversing the channel over the simulation period.

On each side of the vestibule, a cylindrical reservoir with radius 30 Å and an adjustable height was placed. A fixed number of sodium and chloride ions were placed in each reservoir, and the height of the cylindrical reservoir was adjusted to give a desired ionic concentration. As ions were forbidden to approach the wall of the reservoir within 1 Å, the effective radius of the cylindrical reservoir was 29 Å. For example, if 13 sodium and 13 chloride ions were placed in each reservoir and the desired ionic concentration was 300 mM, the height of each of the two cylindrical reservoirs was adjusted to 22 Å.

7.4 Results

7.4.1 Dipoles in the Channel

In the absence of any dipoles in the protein wall, the potential barrier presented to an ion moving under the influence of an applied potential of 100 mV is shown in Fig. 7.2 (top curve, labeled 0). The potential profile presented to the ion as it moved from outside (left-hand side) to inside (right-hand side) increased slowly, peaking at the center of the cylindrical transmembrane segment (labeled 0 Å), and then decreased steadily as it traversed the second half of the channel. Without the membrane potential, one would have obtained a symmetrical, bell-shaped barrier with a peak height of 14.5×10^{21} J. The presence of the membrane potential had lowered the relative height of the barrier to 3.5×10^{21} J and distorted the shape of the profile to an asymmetrical curve.

Two rings of dipoles, together with an applied electric potential of 100 mV, eliminated the repulsive dielectric force. The number accompanying each curve in Fig. 7.2 represents the total strength of 4 dipoles ($\times 10^{-30}$ Cm) in each ring. Since there were two rings of dipoles, one at $z = -5$ Å and the other at $z = +5$ Å, the strength of dipoles placed on the entire channel wall was twice the value indicated in the figure. In the presence of dipoles, an ion traversing from outside to inside would encounter an attractive potential throughout its trajectory. With each stepwise increase in dipole strength, what used to be a potential barrier became a potential well whose depth

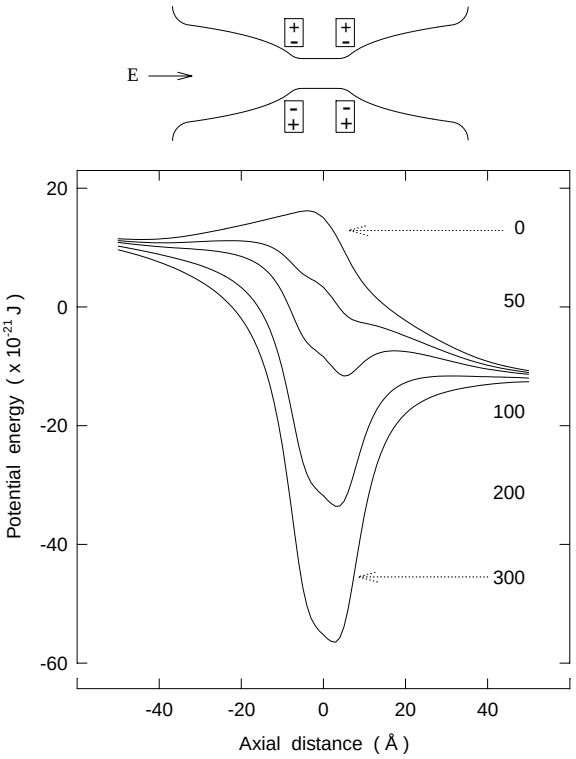

Figure 7.2: Changes in the potential profile with dipole strength. The potential barrier presented to a cation is plotted against its position along its trajectory. A membrane potential of 100 mV was applied such that inside (right-hand side) was negative with respect to outside (left-hand side). The value at each position was computed from a numerical method of solving Poisson's equation. The uppermost curve, labeled 0, was obtained in the absence of dipoles on the channel wall. The next four curves represent the potential profiles encountered by a cation traversing the channel in the presence of dipoles with strengths of, respectively, 50, 100, 200 and 300×10^{-30} Cm. The approximate positions of four of the 8 dipoles in the channel are indicated in the inset. The remaining four dipoles are on the orthogonal plane to those shown.

increased with the strength of dipole moments.

In Fig. 7.3, the number of ions that traversed the channel under the driving force of 100 mV during a simulation period of 0.45 μs (4.5 million time steps) is converted to current in pA and plotted against the dipole strength. On the right-hand ordinate of Fig. 7.3, current in pA are converted to conductance in pS at the physiological concentration of 150 mM. Since the current in these ranges of ionic concentrations increases almost linearly with concentration (see later), such an extrapolation of conductance results is justified. With no dipoles placed on the channel wall, the number of sodium ions that traversed from outside to inside in 0.45 μs was 10, which corresponds to a current of 3.6 pA. The net current increased rapidly with the increasing dipole strength up to 100×10^{-30} Cm (filled circles in Fig. 7.3). The number of ions crossing the channel increased further with a further increase in the dipole strength, but many ions were also traversing in the opposite direction, against the direction of the applied electric field. The current flowing from inside to outside is indicated as open circles in Fig. 7.3. As a result, the net current actually decreased as the dipole strength was increased further from 300 to 600×10^{-30} Cm.

7.4.2 Ionic Concentrations in the Channel

In the volume of our model channel, which is 2.16×10^{-26} m^3, there would be 720 water molecules. At a concentration of 300 mM, a similar bulk volume would contain 4 sodium and 4 chloride ions. Here we examine the number of sodium and chloride ions inside the channel under various conditions. To compute the average number and concentration of sodium and chloride ions inside the channel, we divided the model catenary channel, whose length is 80 Å, into sixteen 5-Å-thin sections as shown in the inset of Fig. 7.4. The volumes of the slices from the outermost layer to the smallest layer in the transmembrane segment are 2.94, 2.18, 1.88, 1.54, 1.16, 0.71, 0.25 and 0.15×10^{-27} m^3.

In the absence of a membrane potential and dipoles in the protein, ions were virtually excluded from entering the vestibule neck owing to the repulsive dielectric force presented to them by the dielectric wall. In Fig. 7.4 A and Fig. 7.4 B, the time averages of sodium and chloride concentrations in the channel are illustrated. The number of ions present in each layer per unit time was first tabulated (filled and open circles) and then the concentration in each layer was derived by taking into account its volume. The average ionic concentration in each of the two outermost layers was about 10% lower than that in the adjoining reservoir, which was 300 mM. The ionic concentration in successive layers declined progressively, dropping to less than 10% of the reservoir value in the neck region.

When a membrane potential of 100 mV was applied across the channel, such that the right-hand side reservoir was made negative with respect to the

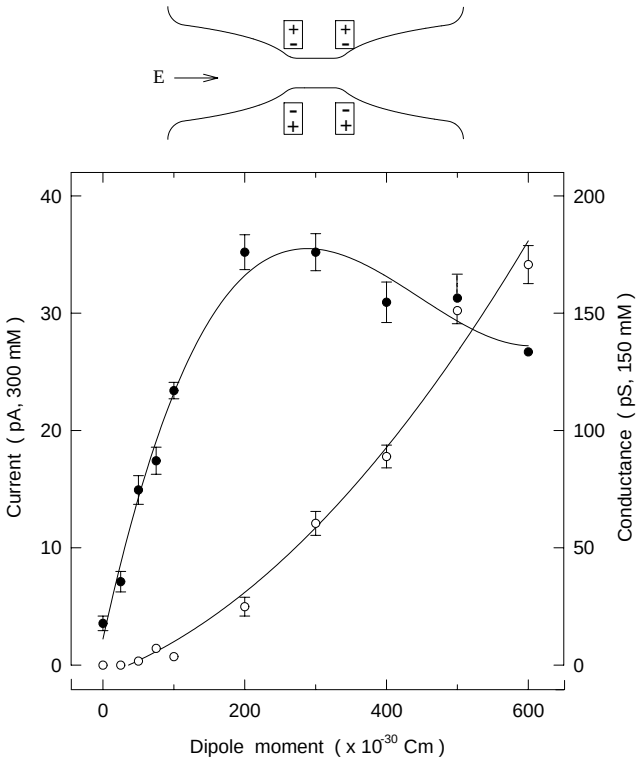

Figure 7.3: Channel conductance as a function of dipole strength. The magnitudes of sodium currents flowing across the channel in the presence of a membrane potential of 100 mV are plotted against strengths of dipoles. The ionic concentration of the reservoir was 300 mV. The left-hand side of the ordinate indicates the current in pA at 300 mM, whereas the right-hand side of the ordinate indicates the conductance in pS at 150 mM. The filled circles show the net current, *i.e.*, the sum of currents in both directions, which flows from outside to inside. The open circles show the current flowing against the potential gradient, namely, from inside to outside. Simulation time for each data point was 0.45 μs, except the value for 100 $\times 10^{-30}$ Cm, which was 2 μs. The points were fitted with a polynomial function.

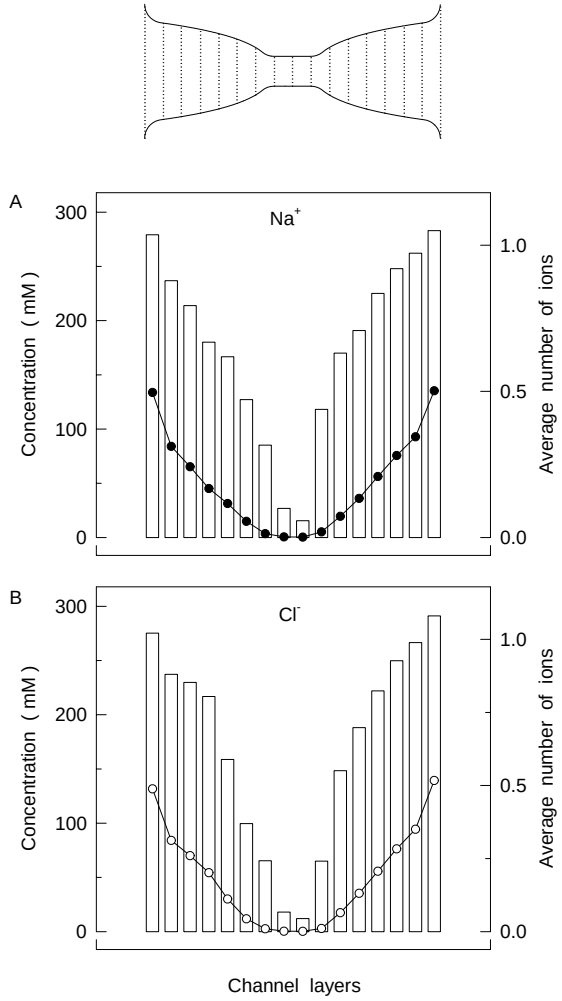

Figure 7.4: Concentrations of sodium and chloride ions in the channel. The model channel was divided into sixteen 5-Å-thick sections, as indicated in the inset, and the average number of ions present over the simulation period of 0.45 μs in each section was tabulated (filled and open circles). The ionic concentration in each section was then calculated by dividing the average number of ions in each section by its volume (bars). The concentration of sodium (and chloride) ions in the reservoirs was 300 mM in this and the following 3 figures. With no dipoles on the channel wall and no applied electric field, the probability of sodium ions (A) and chloride ions (B) being in each section decreased steadily with its distance from the reservoir.

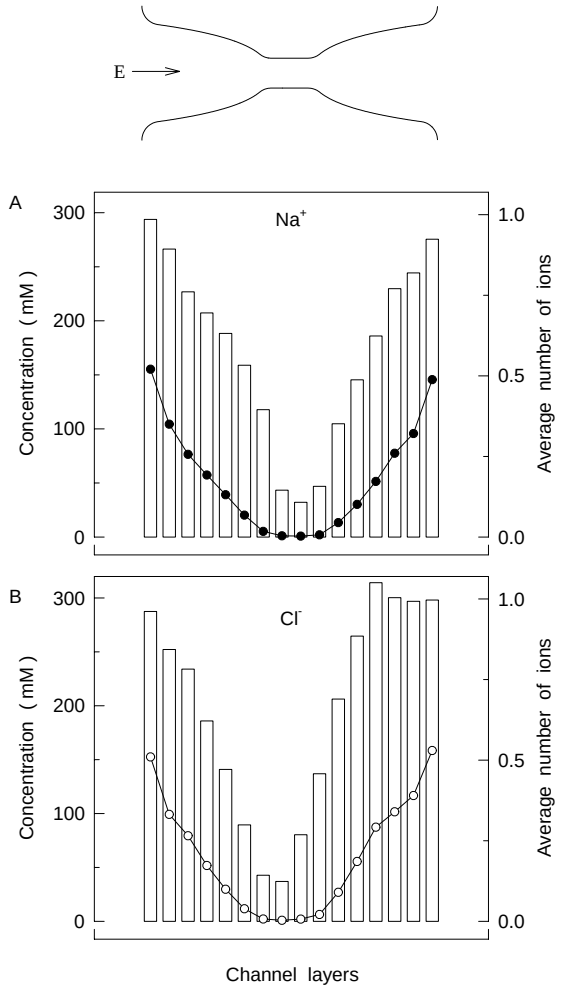

Figure 7.5: Concentrations of sodium and chloride ions in the channel in the presence of a membrane potential E. When a membrane potential of 100 mV was applied, as shown in the inset, there was a small increase in the concentration of sodium ions in the left-hand side vestibule (A) and a similar but slightly larger increase in chloride ions in the right-hand side vestibule (B). The difference is due to the larger diffusion coefficient of chloride ions compared to that of sodium ions.

left-hand side, there was a small but consistent increase in the concentration of sodium ions in the left vestibule and in the concentration of chloride ions in the right vestibule (Fig. 7.5). Other than this small asymmetry in the concentrations and a slight increase in the probability of ions being present in the constricted segment, the applied field had little effect on the average concentrations in the channel. A drastic change in the pattern of charge densities occurred when, instead of applying an electric potential across the channel, two rings of dipoles were placed on the channel wall. As shown Fig. 7.6, there was a marked increase in the concentration of sodium ions in the constricted region of the channel. Sodium ions entering the channel occasionally would become detained in the potential well created by the dipoles on the wall. Some ions travelled from one well to the other and drifted across to the other side, but because there was no potential gradient, the number of ions drifting in one direction (11.7 ± 1.3 pA) was about the same as that in the opposite direction (10.7 ± 1.3 pA).

To mimic the concentration gradient in the channel during its open state, we placed an energy barrier of 1.5 kT_r at the constricted segment and applied a membrane potential of 100 mV. As shown in Fig. 7.7, the sodium concentration in all layers of the channel was approximately constant under these conditions and ions steadily moved from outside to inside, without being detained by the dipoles on the channel wall. In contrast, chloride ions were virtually excluded from entering the inside of the channel (Fig. 7.7 B). The conductance of the channel under this condition was 78 ± 4 pS at 150 mM (or 15.5 ± 0.7 pA at 300 mM), and no sodium ions traversed against the potential gradient.

7.4.3 Current-Voltage Relationships

The current-voltage relationships obtained from excised single channels are in general ohmic, although some show pronounced inward or outward rectification. The reversal potential observed in asymmetric ionic solutions closely matches that predicted by the Nernst equation. Here we show how the presence of an energy barrier in the channel can distort the linear current-voltage relation.

The current increased linearly with the applied voltage, as shown in Fig. 7.8 A, when there was no additional potential barrier in the channel presented to ions for penetrating the transmembrane segment. In this and all subsequent current-voltage curves, we used the total strength of 4 dipoles in each ring of 100×10^{-30} Cm. The core conductance of the channel, deduced from the regression line of the form, $I = \gamma\, V$, fitted through the data points, was 232 ± 4 pS (or 116 pS at 150 mM). When an energy barrier of 3.0 kT_r was erected at the entrance of the constricted segment, the current was attenuated, but not by a constant proportion at all voltages. For example, the currents in the absence and presence of this barrier at

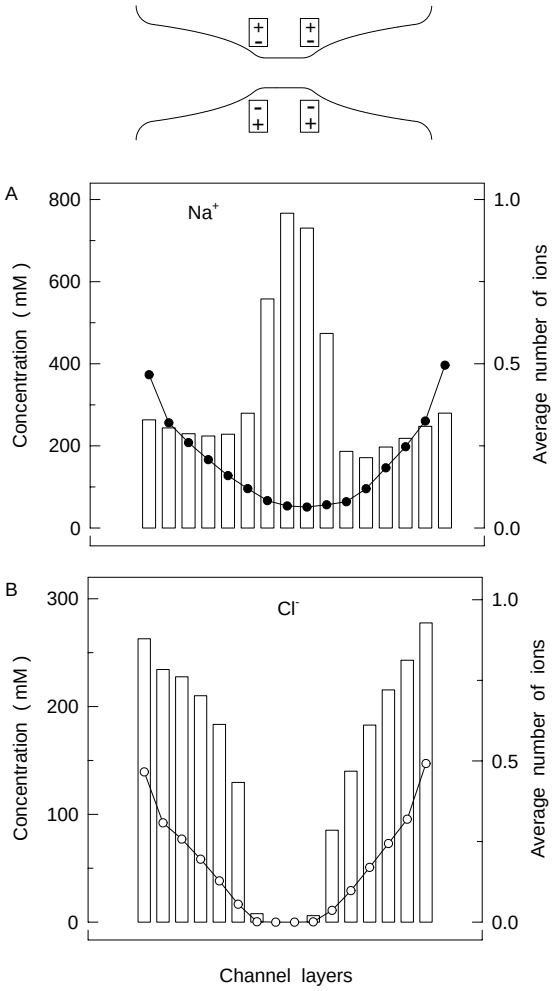

Figure 7.6: Concentrations of sodium and chloride ions in the channel in the presence of two dipole rings. Each dipole ring, with the total moment of 100×10^{-30} Cm, was placed in the positions indicated in the inset. There was a large increase in the concentrations of sodium ions in the innermost sections of the channel (A). In contrast, chloride ions were excluded from the innermost sections (B).

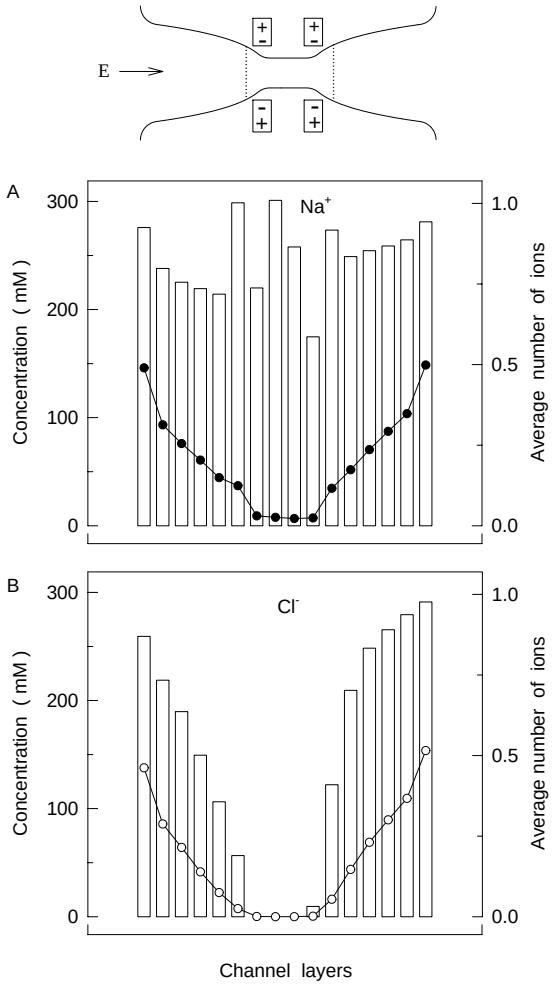

Figure 7.7: Concentrations of sodium and chloride ions in the presence of dipoles and an applied electric field. Two potential barriers of 1.5 kT_r were placed at the positions indicated in the inset. With two rings of dipoles canceling the repulsive dielectric force and a driving force provided by a membrane potential of 100 mV, sodium ions steadily traversed the channel. The concentrations of sodium ions in all sections of the channel remained approximately constant (A). In contrast, chloride ions were virtually excluded from the transmembrane sections (B).

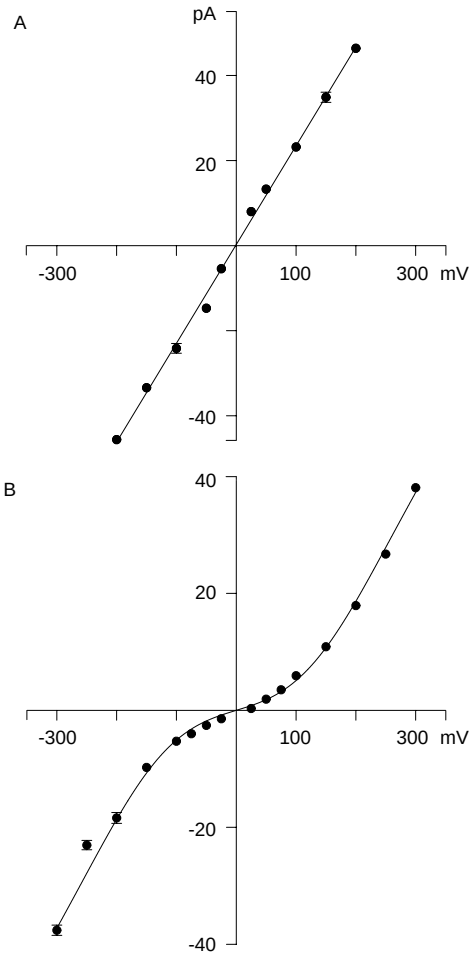

Figure 7.8: Current-voltage relationships obtained with symmetrical solutions. (A) The currents flowing across the channel that had no potential barrier near the entrance of the transmembrane segment were measured at different applied potentials. Two rings of dipoles, each ring with the strength of 100×10^{30} Cm, were placed on the channel wall. The current-voltage relationship obtained under these conditions is ohmic. The slope of the line drawn through the data points is 232 ± 4 pS. (B) When potential barriers 3.0 kT_r was erected, the current-voltage relationships became nonlinear. The data points were fitted with a modified Ohm's law which takes the barrier into account (see Eq. (7.1). The values of γ and β used to fit the curve were, respectively, 142 ± 4, and 3.5 ± 0.4. The simulation period used to obtain each data point was 1 μs.

200 mV were, respectively, 46.0 pA and 18.2 pA (39.6%). With the applied potential of 50 mV, however, the current was reduced from 14.0 pA to 2.2 pA (15.7%), thus indicating that the barrier of the same height became less of an impediment when the driving force was large. With a 3.0 kT_r barrier, the current-voltage relationship became nonlinear, deviating markedly from Ohm's law, as shown in Fig. 7.8 B. The solid line fitted through the data points in Fig. 7.8 B was calculated from the Pöschl-Teller function of the form, $I = \gamma\ V/[1 + \beta\ \text{sech}\ x]$, where $x = eV/V_B$ and V_B is the barrier height. The justification for fitting the data with this function is given in section 7.2.1. The values of γ and β used to generate the curves shown in solid lines are given in the figure legend.

7.4.4 Conductance-Concentration Curve

Experimentally, current across a biological ion channel increases monotonically with an increasing ionic concentration initially and then saturates with a further increase in concentration [31]. Saturation of channel currents occurs when there is a rate-limiting permeation process that is independent of ionic concentrations. For example, an ion arriving near the constricted membrane segment will be detained there for a period of time if, before traversing the narrow pore, it needs to gain sufficient kinetic energy to climb over an energy barrier. The reason for the presence of such a barrier is explained in the section 7.1.3.

In Fig. 7.9, the conductance of the channel is plotted against the concentrations of sodium ions in the reservoirs. The two reservoirs contained an equal number of sodium-chloride pairs, and an applied membrane potential of -100 mV provided the driving force for sodium ions to move inward. The presence of 2 rings of dipoles, with their negative poles pointing to the lumen, ensured that the channel was selectively permeable to sodium ions. When the channel had no potential barrier, the ionic current carried by sodium ions increased linearly with concentration, as shown in Fig. 7.9 A. Since the magnitude of the current in this series of simulations was large, we used the total simulation period of 0.225 μs for each point shown in Fig. 7.9 A. The linear conductance-concentration relation became distorted when a barrier was placed at 5 Å from each end of the cylindrical pore. Figure 12B illustrates the conductance-concentration curve obtained from the channel with a step potential barrier of 3.0 kT_r. The ordinate of Fig. 7.9 B is expanded, since the currents were greatly attenuated by the presence of the barrier. At a low ionic concentration, the conductance was nearly proportional to the ionic concentration. As the ionic concentration was increased, however, the conductance increased less with increasing concentrations. We fitted the points with the curve calculated from the Michaelis-Menten equation of the

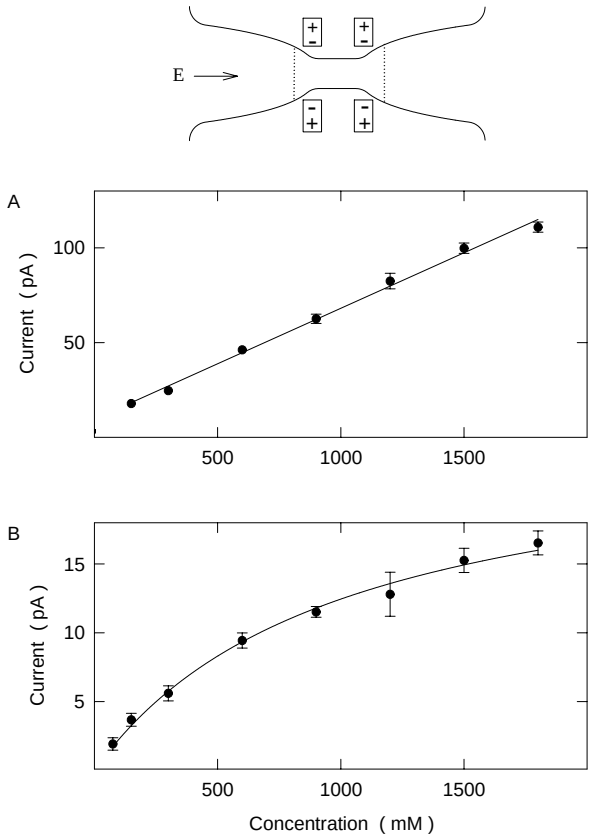

Figure 7.9: Conductance-concentration curve. The ionic concentrations in the two reservoirs were systematically increased while keeping the strength of dipoles and an applied membrane potential constant at 100×10^{-30} Cm and 100 mV, respectively. The number of ion pairs in each reservoir, with the radius of 30 Å, ranged from 3 (for 75 mM) to 78 (for 1,800 mM). (A) With no barrier present, the current increased linearly with ionic concentrations. Each point represents the average of 9 trials, each trial lasting 250,000 time steps or 0.225 μs. (B) When a step barrier, whose height was 3.0 kT_r, was erected at 5 Å from the entrance of the transmembrane segment, the conductance-concentration relation became nonlinear. The current increased linearly with an increasing ionic concentrations at first and then began to saturate. The data points of (B) were fitted with Eq. (7.7). The simulation period for each point in (B) were 1 μs, except for those representing 1.2, 1.5 and 1.8 M, for which the simulation periods of 0.3 μs were used.

form

$$I = \frac{I_{\max}}{1 + K_s/[c]} \tag{7.7}$$

where $I_{\max}$ and K_s are the fit parameters. For the solid line drawn through the data points of Fig. 7.9 B, the numerical values of these two parameters are $I_{\max} = 25 \pm 5$ pA and $K_s = 996 \pm 351$ mM. In section 7.2.2, we give a possible physical interpretation of Eq. (7.7).

7.5 Discussion

The idea that dipoles are needed to allow free permeation through the model channel is confirmed by the results in this chapter, with the proviso that some current flows even without dipoles. In the absence of dipoles permeation through the channel is severely retarded: the conductance is around 20 pS as compared to a maximum of around 175 pS with dipole rings (Fig. 7.3). This reduction in conductance can be attributed to the electrostatic energy barrier created by the dielectric boundary in the absence of dipoles (Fig. 7.2). This barrier reduces the concentration of ions in the neck region to around 40 mM, compared to 300 mM in the reservoirs (Fig. 7.5). However, when dipole rings are added the energy barrier is replaced by an energy well (Fig. 7.2), the concentration in the neck region increases to around 750 mM (Fig. 7.6), and a substantial current can flow (Fig. 7.3). The results of the long simulations confirm the picture hinted at by the ion trajectories of the previous chapter, but add detail and provide quantitative predictions.

These results also give support to another explanation for the presence of ions in the neck region of channels: that they serve to increase the concentration of ions in the neck, increasing conductance in the narrowest part of the channel, so overcoming a bottle-neck and producing a channel with a large conductance [31]. Even the small energy well created by 100×10^{-30} Cm dipole rings increases the concentration of cations in the neck region to 2.5× the bulk concentration. Dipole rings of 200×10^{-30} Cm strength produce a much bigger well and increase conductance from 115 pS to 175 pS. However, increasing dipoles beyond this strength does not increase conductance, and actually reduces it slightly for strengths of 400×10^{-30} Cm or more (Fig 7.2). The two explanations for the dipoles need not be mutually exclusive: it is quite possible that dipoles in the neck region of a channel serve firstly to overcome the membrane energy barrier and allow conductance, and secondly to increase ion concentration in the narrowest part of the channel and increase conductance through this bottle-neck. Indeed if permeation through the channel is considered to be one-dimensional, and entropy is included, then the narrow neck region becomes an entropic barrier in addition to the electrostatic membrane barrier, and dipoles are needed to overcome

the combined barrier. This may explain why increasing the strength of the dipoles beyond a certain point does not increase conductance. Note that the simulations are three-dimensional, so that the entropic effects of a narrowing channel emerge implicitly from the motion of the ions, and do not need to be included explicitly.

Shielding by counter-ions seems to be having some effect, but does not completely remove the electrostatic barrier. This can be seen by comparing concentrations in the neck region with the electrostatic energy profiles. Without dipoles the height of the barrier is around 4 kT which, by applying the Boltzmann factor, would suggest a dilution to 1/50 bulk concentration or around 6 mM for both cations and anions. In Fig. 7.4, however, the concentrations are around 20 mM, suggesting that shielding has reduced the barrier by about 30%. Dipoles of 100×10^{-30} Cm create a well of around 2.5 kT, which should increase their concentration by a factor of 12, but Fig. 7.6 shows that the increase is only by a factor of 2.5, suggesting that interactions with other ions have reduced the depth of the well to about 1 kT. Fig. 7.5 is interesting, in that the applied field reduces the height of the barrier to 2 kT (Fig. 7.2), which by the Boltzmann factor suggests a concentration of around 40 mM, which is what is seen in the figure. This might indicate that shielding has a much smaller effect when current is flowing and ions are moving through the channel, but it is difficult to be sure, as the use of the Boltzmann factor is inappropriate in this non-equilibrium situation.

Without an additional energy barrier both current-voltage (Fig 7.8) and conductance-concentration (Fig 7.9) curves are linear, indicating that ions navigate the channel independently, without multi-ion interactions playing an important role. When an sharp energy barrier is added in the neck region both curves become non-linear. The conductance-concentration curve shows saturation with increasing concentration, and can be fitted to the Michaelis-Menten equation. The current-voltage curve shows a particular pattern of non-linearity, with a switch from a region of lower conductance to one of higher conductance at around 100 mV of applied potential. This curve can be fitted to a Pöschl-Teller function, as described in section 7.2.1. Thus, without an energy barrier the model is of a high-conductance single ion channel with linear conductance characteristics, while with energy barriers the model predicts a lower conductance and specific types of non-linearity.

Chapter 8

Multi-Ion Channel

In this chapter we describe the construction of an approximate model of a potassium channel and its use to perform BD simulations. The model is based on the structure of the KcsA channel as described by Doyle et. al. [21]. This is done with the primary aim of seeing if it is possible to build a working model of a multi-ion channel using only a diffusive mechanism. A secondary aim is to test the plausibility of some of the conductance mechanisms proposed by Doyle et. al., but since these mechanisms are deduced in a quite straightforward way from the experimental structure, this might equally be regarded as a test of the plausibility of our model and techniques.

Although their gating characteristics differ, most potassium channels show similarities in amino acid sequence, conductance characteristics, selectivity, and blocking agents. These common characteristics identify them as a group and strongly suggest a common pore structure. Thus, even though KcsA is a bacterial channel, its structure can be taken as representative of the pore structure of all the potassium channels with similar characteristics. The conductance characteristics of potassium channels, specifically ionic flux coupling and saturation at high concentrations, are strong evidence that potassium channels contain between 2 and 3 ions when conducting. They are also taken as evidence that potassium channels contain binding sites, and that conductance is by hopping between these sites, with any diffusion that occurs being irrelevant or incidental (see chapter 14 of Hille [31]). This is because the theories that best describe these characteristics (RRT and the Michaelis-Menten mechanism) are theories about chemical reactions which, as applied to enzymes, involve the binding of a substrate to an enzyme. The explanation in terms of binding sites is reasonable, given that no diffusion based theory has been able to adequately explain conductance in multi-ion channels, but it does not take into account the theoretical problems with RRT as applied to channels (see section 2.1), and does not explain the far greater turnover rate of channels compared to enzymes and carriers (see section 1.2 and chapter 11 of Hille [31]). By attempting to build a diffusion

based model of a multi-ion channel we hope to shed some light on this issue.

The structure of the KcsA channel contains several clues to its conductance mechanisms [21]. At the top (extracellular) end of the channel is a very narrow, 12 Å long section of pore lined by hydrophilic protein backbone much like a gramicidin pore, although the protein chains are straight, not arranged in a helix. This is recognizably a selectivity filter and must hold the key to explaining the extreme selectivity of potassium channels. Doyle et. al. suggest a possible mechanism, but this cannot be investigated by the techniques described here, as macroscopic electrostatics completely ignores the subtle close-range interactions essential for selectivity between ions of the same valence (see section 1.2). The x-ray crystallography used to find the structure of the channel also shows the preferred positions of ions in the pore. There are two such positions in the selectivity filter, located near each end, 7.5 Å apart. These could be interpreted as binding sites, specific locations with a high affinity for potassium ions, but this does not readily explain the high conductance of the channel, as a hop of 7.5 Å (carrying the intervening water with it) seems unlikely, and the selectivity filter is too narrow for diffusion to be considered irrelevant. The interpretation of Doyle et. al. is different: they suggest that the whole selectivity filter has a high affinity for potassium ions, and would trap a single ion, preventing conductance. However, the two ions in the filter destabilize each other by electrostatic repulsion (hence their locations near the ends of the filter), and this allows ions to escape and conductance to occur. We test the plausibility of this mechanism in our BD simulations by placing small dipoles representing carbonyl groups around the model selectivity filter. This creates the necessary high affinity for cations, and transport is provided by the simulated diffusion of the BD motion algorithm.

This model of the selectivity filter may be quite unrealistic. The real carbonyl groups have some freedom to move, a hydrogen bond is not completely representable as a dipole interaction, and calculations by macroscopic electrostatics in such a confined space can be no more than an estimate. The selectivity filter may be more like a series of 4-6 connected binding sites than a continuous attractive region, transport might be through a series of short hops rather than by diffusion, and the single file nature of the filter means that ions and water should move in a coordinated manner, whatever the transport mechanism. All of these issues need to be studied using MD or similar microscopic simulation techniques. However, despite these reservations, and crude as it is, the BD model captures the essential features of the proposed mechanism: a selectivity filter with a high affinity for ions, and mutual destabilization by long-range electrostatic repulsion.

Below the selectivity filter lies a central cavity, and below that an inner pore leading to the cytoplasmic mouth of the channel. The central cavity is an elongated spheroid, about 10 Å across and 12 Å long. The inner pore is around 18 Å long and wide enough for a potassium ion to move

through 'and still remain mostly hydrated' [21]. The linings of both of these regions are predominantly hydrophobic, which raises the question of how the electrostatic barrier created by the membrane is overcome. Doyle et. al. propose mechanisms to reduce the barrier. They suggest that the central cavity and inner pore provide water to surround the ion and thus reduce the barrier, while the hydrophobic walls do not interact greatly with the ion, allowing it to diffuse without impediment. The wider cavity is in the centre of the pore, providing the most hydrating water where the barrier is greatest. They also observe that the pore helices (four short alpha helices that support the selectivity filter) point directly towards the central cavity and (as do all alpha helices) posses significant dipole moments. The negative ends of these large dipoles are closest to the central cavity, and thus they are expected to attract cations. Another preferred ion position is located at the centre of the cavity, although it is more diffuse than the ones in the selectivity filter: this supports the idea that the water filled cavity and helix dipoles overcome the membrane barrier and create instead an energy well which attracts ions. Doyle et. al. point out that this preferred ion position in the cavity does not represent a binding site in the conventional sense, but rather 'a hydrated cation cloud'.

Three-dimensional BD seems well suited to the task of investigating conductance in the inner pore and central cavity. The mechanism that Doyle et. al. propose for transport in this region is diffusion, with the electrostatic barrier overcome by a combination of shielding by water molecules and long range electrostatic interactions with the channel structure. These are exactly the physical phenomena that the methods described in this thesis are designed to reproduce (although the accuracy of this reproduction may be far from perfect due to the use of macroscopic electrostatics and other simplifications). This region of the channel represents around 70 percent of its length, and if Doyle et. al. are right about the purpose of the central cavity and helix dipoles, is relevant to the channel's conductance. Of course the conductance of a channel depends on its entirety, not just particular regions, so the selectivity filter must be included in any simulation expected to reproduce conductance. Although our model of the selectivity filter is necessarily crude, and other techniques are better suited to investigating this region of the channel, the conductance mechanism proposed by Doyle et. al. is not incompatible with a BD simulation or macroscopic electrostatics.

8.1 Model

This model was derived from the structural descriptions and figures in the paper by Doyle et. al. [21], not the molecular coordinates: at the time it was built we did not have the ability to analyze such coordinates to produce a model.

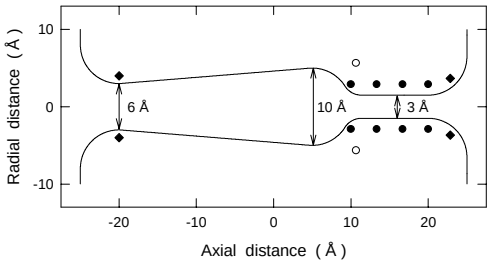

Figure 8.1: Idealized potassium channel. The channel shape is generated by rotating the curves outlined along the symmetry z-axis by 180°. The positions of the negative ends of the dipoles in the channel wall are indicated: filled circles show 8 of the 16 carbonyl oxygen atoms; open circles the helix dipoles, and filled diamonds, the mouth dipoles.

8.1.1 Shape of the Channel

The shape of our model channel is a simple, geometric representation of the pore structure (see Fig. 8.1). The three-dimensional shape of the channel is generated by rotating the curves shown around the symmetry axis (z axis) by 180°. The total length of the model channel is 50 Å, compared to 45 Å for the real channel. The model channel is slightly longer due to the need to add curved sections at each mouth of the channel (the iterative method of solution does not deal well with sharp corners). These curves are quarter circles with a radius of 5 Å.

The selectivity filter is represented by a cylindrical section 1.5 Å in radius and 10 Å long. The real selectivity filter is around 12 Å long, but in our model the inner 2 Å of the curved extracellular mouth is very narrow (maximum radius 1.9 Å), and can be regarded as part of the filter. The radius of the selectivity filter is deduced from the ions that can pass through it (see chapter 13 of Hille [31]). Potassium ions (radius 1.33 Å) can pass through easily, as can rubidium ions (radius 1.48 Å). Caesium ions (radius 1.69 Å) can enter the filter but tend to get stuck: presumably some areas of the filter are wider than others, and the filter has some flexibility. For our

very simplified model for use with BD, 1.5 Å seems a reasonable average radius.

The central cavity and inner pore are represented in our model by a hemisphere and a truncated cone. The hemisphere has a radius of 5 Å, corresponding to the 10 Å width of the central cavity. The truncated cone is 25 Å long and has a radius of 5 Å where it meets the hemisphere reducing to 3 Å where it meets the cytoplasmic mouth. The cytoplasmic mouth of the channel admits tetraethylammonium (TEA) ions to the inner pore when the channel is open [21]. This suggests a width of at least 5-6 Å, since a TEA ion (chemical formula $(CH_3)_4N^+$) consists of four carbon atoms in a tetrahedron bonded to the central nitrogen atom, and carbon atoms have a hard-sphere radius of 1.4 Å. The total length of hemisphere and cone is 30 Å, corresponding to the total length of central cavity (12 Å) and inner pore (18 Å) in the real channel.

Small curved sections join the selectivity filter, hemisphere, truncated cone, and cytoplasmic mouth without sharp corners. In our coordinate system the model channel runs from $z = -25$ Å on the cytoplasmic side to $z = 25$ Å on the extracellular side. The narrowest point in the inner pore is at $z = -20$ Å, the centre of the cavity is at $z = 5$ Å, and the selectivity filter runs from $z = 10$ Å to $z = 22$ Å.

8.1.2 Dipoles

The positions of fixed charges and dipoles in our model are based, where possible, on the structure described by Doyle et. al. We regard their strengths as adjustable parameters, however. This is done in order to give the model flexibility to cope with the possible inaccuracies in the calculation of energy barriers and wells which might arise due to the use of macroscopic electrostatics. We place four sets of dipoles in the model protein wall, each with four-fold symmetry around the z axis. Two of these sets are mouth dipoles, representing the negative charges at each entrance of the channel reported by Doyle et. al. [21]. The negative ends of these dipoles are placed at $z = 22.83$ Å and $z = -20$ Å, just inside the protein wall (filled diamonds in Fig. 8.1). For each mouth dipole we place a counter-charges 5 Å further in, but this is a guess, as it is not clear from the descriptions or diagrams in the paper whether there are counter-charges for the negative charges near the channel entrances, or if so where they are. The third set are the helix dipoles, representing the dipole moments of the pore helices. The position and orientation of these dipoles is known from the structure: their negative ends are 8 Å from the centre of the cavity (open circles in Fig. 8.1), they are aligned at 45° from the channel axis, and they point directly towards the centre of the cavity [21]. Their length can be deduced to be 16 Å based on number of residues in each helix. The fourth set are the carbonyl dipoles, representing the carbonyl groups that line the selectivity filter. As explained

above, these are only a rough approximation of the hydrophilic lining of the filter. Four carbonyl dipoles are placed along the selectivity filter, spaced evenly along a distance of 10 Å and oriented perpendicularly to the z axis. With the four-fold symmetry around the z axis this gives a total of 16 small dipoles. The dipoles are located at $z = 10$, 13.33, 16.67 and 20 Å with the negative pole of each placed 1 Å from the boundary (filled circles in Fig. 8.1), and the positive pole 1.2 Å further away. The dipole length of 1.2 Å is chosen to correspond to that typically used for carbonyl groups in MD simulations [11].

8.1.3 Brownian Dynamics

We use our multiple time step algorithm (see section 7.3.2) to simulate the motion of ions more accurately and allow non-reflective repulsion from the walls in the narrowest regions of the pore. A short time step of 2 fs is used in the mouth regions of the channel and the selectivity filter. A long time step of 100 fs is used elsewhere. Specifically, there are two short time step bands, $-25 < z < -15$ and $7.5 < z < 25$, comprising both entrances and the selectivity filter. If an ion is in one of these bands at the beginning of a 100 fs period, it is simulated by 50 short steps instead of one long step; so synchronization between the ions is maintained. Long-range forces are calculated normally at the start of the 100 fs period, and are assumed to be constant throughout. Short range forces are calculated every 2 fs. Coulomb interactions between ions are calculated at the start of each long time step except where both ions are in the same band, when they are recalculated for each 2 fs step. Forces due to the Born energy barriers described in the next section are also calculated every short time step.

The short range forces represent the repulsion that occurs when electron clouds overlap. They are approximations, primarily intended to prevent ions from interpenetrating each other or the protein walls, but they do provide more accurate motion than the reflection algorithm which serves this purpose in the long time step regions. We do not expect that short range forces have a large role in conductance in the inner pore and central cavity, as these regions have a hydrophobic pore lining. Short range forces obviously *are* important in the selectivity filter, but our techniques cannot reproduce them accurately, so we must be content with a crude model of this region. As explained above, even such a simplified model may well be useful.

The ion-ion interaction is given by the potential function

$$U_{II}(r_{12}) = \frac{F_0}{9} \frac{(R_1 + R_2)^{10}}{r_{12}^9}, \tag{8.1}$$

where r_{12} is the ion-ion distance, R_i, $i = 1, 2$, are the Pauling radii of the ions and F_0 is the magnitude of the short range force at contact. For the

ion-protein wall potential U_{IW}, a similar form is used

$$U_{IW}(r) = \frac{F_0}{9} \frac{(R_i + R_W)^{10}}{(\rho(z) + R_W)^9}, \tag{8.2}$$

where R_W is the radius of the atoms making up the wall and $\rho(z) = R_C(z) - r$ is an estimate of the distance from the ion to the channel wall, r being the radial coordinate of the ion and $R_C(z)$ being the radius of the pore at the ion's z coordinate. We use $R_W = 1.4$ Å (the Pauling radius of a carbon atom) and $F_0 = 2 \times 10^{-10}$ N (estimated from the ST2 water model used in molecular dynamics [69]).

8.1.4 Dielectric Constant

Conditions in the pore may be quite different from those in a bulk electrolyte solution (see section 3.1.4) so we regard the dielectric constant in the pore as an adjustable parameter. Unfortunately, due to the limitations of our iterative method, the dielectric constant for the model water must be the same throughout the simulation: the dielectric constant can only change at dielectric boundaries, and the iterative method does not give meaningful results if an ion crosses such boundaries. This means that when we reduce the dielectric constant in the pore, the dielectric constant in the reservoirs is also reduced, whereas in reality it should probably be close to the bulk value. One consequence is that the energy barrier due to the ion moving from a high dielectric strength region (the reservoir) to a lower one (the pore) is not reproduced by our electrostatic calculations.

In an attempt to compensate for this omission, we add an extra energy barrier in the form of a step at each entrance of the channel. The height of this energy barrier is given by the Born energy (see section 3.1.2)

$$E_{\mathrm{B}} = \frac{q^2}{8\pi\epsilon_0 R_{\mathrm{B}}} \left(\frac{1}{\epsilon} - \frac{1}{80} \right). \tag{8.3}$$

We use $R_{\mathrm{B}} = 1.93$ Å which is derived from the estimated enthalpy of hydration for K^+ ions [10]. The shape of the potential step is given by the smooth switching function

$$U_{\mathrm{B}}(s) = (E_{\mathrm{B}}/16)(3s^5 - 10s^3 + 15s) + (E_{\mathrm{B}}/2), \quad s = \frac{z - z_c}{\Delta z}, \tag{8.4}$$

which has continuous first and second derivatives and rises gradually from 0 to E_{B} as s changes from -1 to 1. Here, $z_c = \pm 22.5$ Å is the location of the center of the profile and $\Delta z = \mp 1.5$ Å is its half-width. To give an indication of the barrier heights involved, we note that for $\epsilon = 20$, 40 and 60, $E_{\mathrm{B}} = 5.4$ kT, 1.8 and 0.6 kT, respectively.

8.2 Methods

8.2.1 Energy Profiles

In the results section we calculate both single-ion and multi-ion energy profiles. The potential profile of an ion is constructed by solving Poisson's equation with the ion fixed at a series positions spaced at 1 Å intervals along the z-axis. This is done using the lookup tables in the same way as in the BD simulations. This is a simple process for a single-ion profile, but the channel contains more than one ion while it is conducting, and so we need to be able to calculate energy profiles in the presence of additional ions.

To visualize the shape of the energy barrier an ion encounters as it attempts to enter a channel that is occupied by one or more ions, we have constructed multi-ion energy profiles. We move one of the ions from the intracellular space into the channel in 1 Å steps, holding it fixed at each step. We then allow the other ions in the selectivity filter to adjust their positions so that the force on them will be zero, thus minimizing the total energy of the system. The minimization is performed at each step and the positions of the ions and the total energy are recorded. The total energy corresponds to the total electrostatic energy required to bring in the charge on the ions from an infinite distance in infinitesimal amounts, and it is given by

$$U_{\text{total}} = \sum_i \frac{q_i}{2} \left[2V_{\text{X},i} + V_{\text{S},i} + \sum_{j \neq i} (V_{\text{I},ij} + V_{\text{C},ij}) \right] + U_{\text{B},i}, \tag{8.5}$$

where the indices i and j range over all the ions. The potential terms in Eq. (8.5) are described in section 6.1 and section 8.1.4. The factors of $1/2$ in the middle three terms arise from the integration of charge during build up. Using a modified version of the steepest descent algorithm (see [58]), the total energy of a multiply-occupied channel given in Eq. (8.5) is successively minimized until the forces on the free ions vanish.

8.3 Results

8.3.1 Dipoles and Energy Profiles

As an ion approaches the boundary between an aqueous solution and the protein wall, it experiences an electrostatic repulsion due to induced charges at the boundary. In computing the potential energy of an ion as it moves along the central axis, we assume initially that the dielectric constant ϵ in the reservoirs and the pore is 60. The energy of transition from bulk water, estimated from the Born energy, is incorporated as a potential barrier at the channel entrance as explained in the section 8.1.4.

In the absence of any charge moieties on the protein wall, an ion attempting to traverse the channel encounters a significant energy barrier.

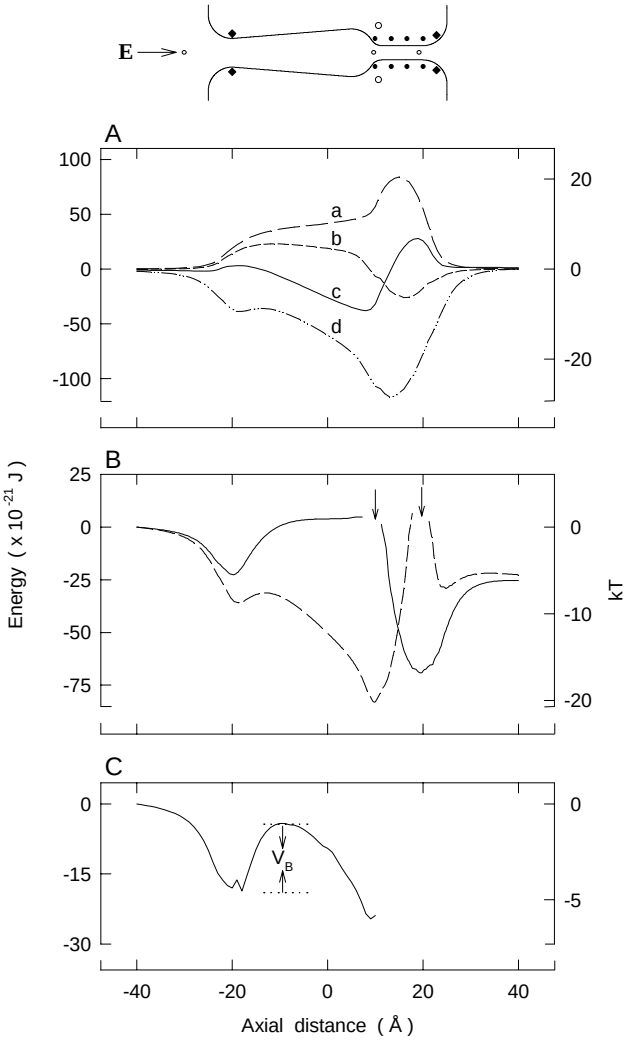

Figure 8.2: Electrostatic energy profile of a potassium ion traversing the channel. (A) The potential energy of an ion along the central axis. The profile **a** is the potential energy seen by the ion, in the absence of any charge moieties on the channel wall, profile **b** is obtained with 4 sets of 4 carbonyl groups (filled circles in the inset), profile **c** is obtained with 4 helix macrodipoles (open circles in the inset), and profile **d** is obtained with the carbonyl groups, helix dipoles and 2 rings of mouth dipoles (filled diamonds in the inset). (B) Potential profiles seen by individual ions while the other is fixed at the equilibrium position (indicated by arrows). The applied field corresponds to a potential difference of about 150 mV between the channel entrances. The first ion is placed at the equilibrium position $z = 10$ Å and the profile seen by the second ion is computed (solid line). The second ion is now placed at $z = 19.75$ Å and the profile seen by the first ion is computed. (C) The potential profile encountered by a third ion, as it moves from left to right. At each fixed position of the third ion, the stable configuration of the first two ions is determined iteratively and then the total energy of the assembly is computed. The strengths of each carbonyl group, mouth dipole and helix dipole are, respectively, 7.2, 30 and 96.3 $\times 10^{-30}$ Cm.

The potential energy at a fixed position of an ion is computed numerically and the calculation is repeated at 1 Å intervals. The profile presented to the ion as it moves from inside (left) to outside (right) increases slowly at first and then rises steeply in the narrow selectivity filter, reaching a peak of 20 kT, as shown in Fig. 8.2 A (curve labeled **a**). Four rings of dipoles, with 4 carbonyl groups in each ring, placed along the selectivity filter, transform a section of the barrier into a well (**b**) as do 4 helix dipoles placed just below the selectivity filter (**c**). As it will be shown later, two sets of additional mouth dipoles are needed to render the channel permeable to ions. When all three sets of dipoles – 16 carbonyl groups, 4 helix macrodipoles and 8 mouth dipoles – are placed along the channel wall, the profile an ion encounters while traversing the central axis of the channel is a deep potential well (**d**).

The potential well created by the dipoles, reaching a depth of nearly 30 kT, attracts cations. An ion, upon entering the channel, will proceed towards the bottom of this well. A second ion entering the channel sees a different profile, altered by the presence of the first ion. The well in Fig. 8.2 A (**d**) is deep enough to hold two ions in a stable configuration. Through an iterative energy minimization procedure, one can determine the equilibrium positions of the pair of ions in the well. The potential profile seen by either ion while the other is fixed at the equilibrium position, in the presence of an applied field of 1.5×10^7 V/m, is shown in Fig. 8.2 B. At these positions (indicated by arrows), the z-component of the force experienced by the ions is zero. The two-ion potential profiles exhibit relatively deep wells that may attract a third ion. In Fig. 8.2 C we show the potential profile seen by a third ion moving into the channel from the left. Here the potential is calculated at a given position of the third ion after finding the equilibrium positions of the first two ions. There is a shallow well near the entrance of the channel, produced by the ring of mouth dipoles. Once in the well, the third ion will be delayed until random Brownian motion allows it to escape. We note here that the potential minimum is along the central channel axis, so that ions are preferentially funneled along it. The repulsive force from the induced surface charges swings into action whenever an ion strays from the central axis, pushing it back to the axis. The corresponding electric potential profile along the radial axis is similar in appearance to a harmonic well, except that it rises much more sharply near the boundary (see Ref. [33]).

From these electrostatic calculations, we deduce that the channel is normally occupied by two cations. Conduction is unlikely to take place unless these ions are resident in the pore to reduce the energy well created by the charge moieties.

8.3.2 Dependence of Conductance on Dipole Strengths

For the channel to conduct ions, there is a narrow range of moments various dipole groups must possess. Using BD simulations, we have determined how the magnitude of currents flowing across the channel varies with dipole strengths and the effective dielectric constant in the channel lumen.

As shown in Fig. 8.3 A, the conductance increases rapidly as the moment of each carbonyl group is increased from 0 to 7.2×10^{-30} Cm. The current begins to decline when the moment is further increased to 14.4×10^{-30} Cm. The three curves illustrated in Fig. 8.3 A are obtained by letting the effective dielectric constant of the pore be 80 (top curve), 70 (middle curve) and 50 (bottom curve). The charge placed on the terminals of each helix dipole and the strength of each mouth dipole are kept constant at 0.6×10^{-19} C and 30×10^{-30} Cm, respectively. In this and subsequent figures, unless stated otherwise, each point is the average of five simulations, each simulation period lasting for 100 ns. The error bar accompanying a data point is one standard error of means and is not shown if it is smaller than the size of the data point. Again, unless noted otherwise, 13 potassium and 13 chloride ions are placed in the left-hand reservoir (representing the intracellular space), whose volume is adjusted so as to give the ionic concentration of 300 mM, and the same number of ions is placed in the right-hand side reservoir (representing the extracellular space). The applied electric field between the two ends of the reservoirs produces a potential difference of about 150 mV, inside positive with respect to outside. The peak current is always obtained when the strength of the carbonyl groups is fixed at 7.2×10^{-30} Cm (2.16 Debye), irrespective of the assumed dielectric constant. In Fig. 8.3 B, the variation of currents with the dipole moment is determined at 3 different applied potentials, 150 mV, 200 mV and 250 mV, while keeping $\epsilon = 60$ throughout. Again the current peaks at about the same dipole strength.

The results of simulations showing the variation of current with the strengths of mouth dipoles (A) and helix dipoles (B) are illustrated in Fig. 8.4. The dipole moment of each carbonyl group in the selectivity filter is kept at 7.2×10^{-30} Cm throughout. The current flowing across the channel is largest when the charge on each of the four helix dipoles is 0.6×10^{-19} C. Similarly, the current is maximum when the strength of each of the mouth dipoles is 30×10^{-30} Cm. Fig. 8.4 reveals, as does the previous figure, that the dielectric constant of the channel has pronounced effect on the permeability of the channel. With optimum pore helix and mouth dipole strengths, $\epsilon = 60$ gives the physiological conductance of approximately 40 pS, as found experimentally [67]. The channel conductance is progressively suppressed when the dielectric constant in the pore is lowered and no conduction takes place, with the driving force of 150 mV, when $\epsilon \leq 40$.

Here and in all subsequent series of simulations, we assume that the channel possesses the strengths of various dipole groups that enables the

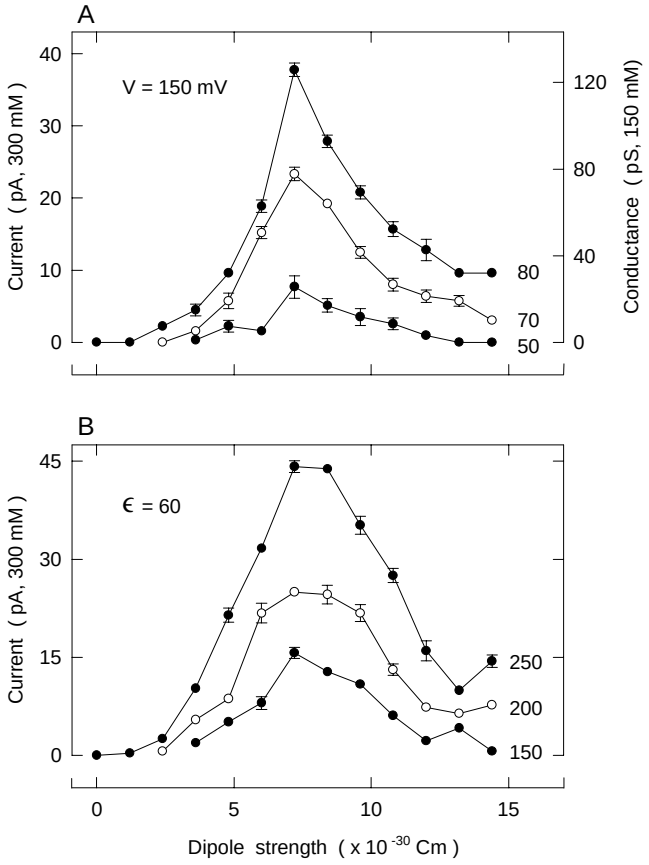

Figure 8.3: Changes in channel conductance with the strength of carbonyl groups. Simulations under various conditions, each lasting 100 ns, are repeated 5 times. The height of each reservoir is adjusted to give an ionic concentration of 300 mM, and inside is made 150 mV positive with respect to outside. The current (in pA) is determined from the total number of ions traversing the channel over the simulation period of 0.5 μs. (A) Keeping the moments of each helix dipole and mouth dipole constant at 96.3 and 30 $\times 10^{-30}$ Cm, the strength of each carbonyl group is systematically changed. The current (in pA) is plotted against dipole strength for three values of the dielectric constant, $\epsilon = 50$, 70 and 80. (B) The current is plotted against the strength of carbonyl groups for three values of applied potential, 150 mV, 200 mV and 250 mV, while keeping ϵ constant at 60.

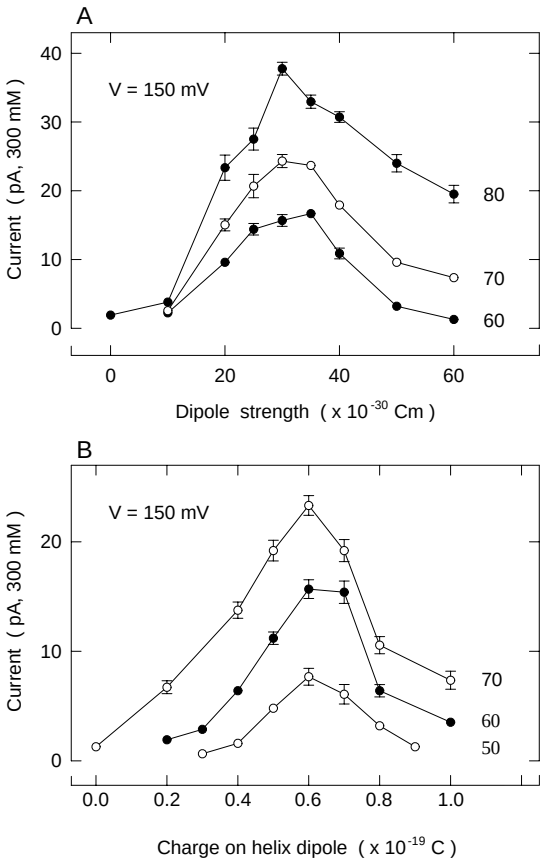

Figure 8.4: Changes in channel conductance with the strength of mouth dipoles (A) and helix dipoles (B). (A) The strength of each mouth dipole is changed systematically while keeping the moments of each carbonyl group and helix dipole constant at 7.2 and 96.3 $\times 10^{-30}$ Cm. The current is plotted against the strength of mouth dipoles for three different values of dielectric constant, $\epsilon = 60$, 70 and 80. (B) The charge placed on each helix dipole is changed systematically while keeping the moments of each carbonyl group and mouth dipole constant at 7.2 and 30 $\times 10^{-30}$ Cm. The current (in pA) is plotted against dipole strength for three values of the dielectric constant, $\epsilon = 50$, 60 and 70.

maximum number of ions to be translocated across the channel for a given driving force, that is, the dipole strengths for each of 8 mouth dipoles, 16 carbonyl groups and 4 helix dipoles are, respectively, 30, 7.2 and 96.3 $\times 10^{-30}$ Cm.

8.3.3 Effects of Dielectric Constant and Diffusion Coefficient on Currents

From the results given in the previous section, it is clear that, for the channel to conduct, the effective dielectric constant ϵ in the pore must be high. In other words, water molecules resident in the pore must not be tightly bound to the protein but be able to rotate relatively freely so as to reduce the interaction energy between the ions and the charges located on the channel wall. In Fig. 8.5, we examine further the influence of ϵ on the magnitude of current flowing across the channel. The depth of the energy well created by dipoles increases as ϵ is lowered. An example of the energy well created by four mouth dipoles located near the channel entrance, when there are two ions resident in the selectivity filter (*c.f.*, Fig. 8.2 C), is illustrated in Fig. 8.5 A. Here, ϵ is assumed to be 30 and a potential of 300 mV is applied across the channel. An ion attempting to cross this well encounters a barrier V_B, the height of which decreases monotonically with increasing ϵ, as shown in Fig. 8.5 B. Increasing the applied potential from 150 mV to 300 mV reduces the barrier height by about 1.5 kT. A steep increase in the barrier height as ϵ is lowered suggests that the channel will not conduct ions if ϵ in the pore is less than 40. The inference drawn from electrostatic calculations is in accord with the results obtained from BD simulations. The current across the channel under the driving force of 150 mV, 200 mV, 250 mV and 300 mV is plotted against ϵ in Fig. 8.5 C. These four curves broadly mirror the way the barrier height increases with ϵ. The current ceases to flow when the barrier height reaches 7 kT.

The diffusion coefficient of potassium ions D_{K} in bulk electrolyte solutions is 1.96 $\times 10^{-9}$ m^2/s. This value is reduced when an ion is diffusing through a narrow tube [64, 17, 47, 68, 5]. The magnitude of the diffusion coefficient of an ionic species depends, among others, on the radius of the cylinder and the composition of the wall. A molecular dynamics simulation of the KcsA channel [6] shows that D_{K} in the wider segment, including the oval chamber, in nearly the same as that in bulk solutions, whereas that in the selectivity filter is on average 1/3 of the bulk value. The following series of simulations are carried out to assess how much the channel conductance is suppressed by a low D_{K} in the narrow filter.

When ions enter the channel segment extending from $z = 7.5$ to $z =$ 25 Å, their motions are determined by a D_{K} that is lower than the bulk value. Fig. 8.6 shows the current across the channel as a function of D_{K} at three different values of dielectric constants, $\epsilon = 60$ (A) and $\epsilon = 50$ and 70

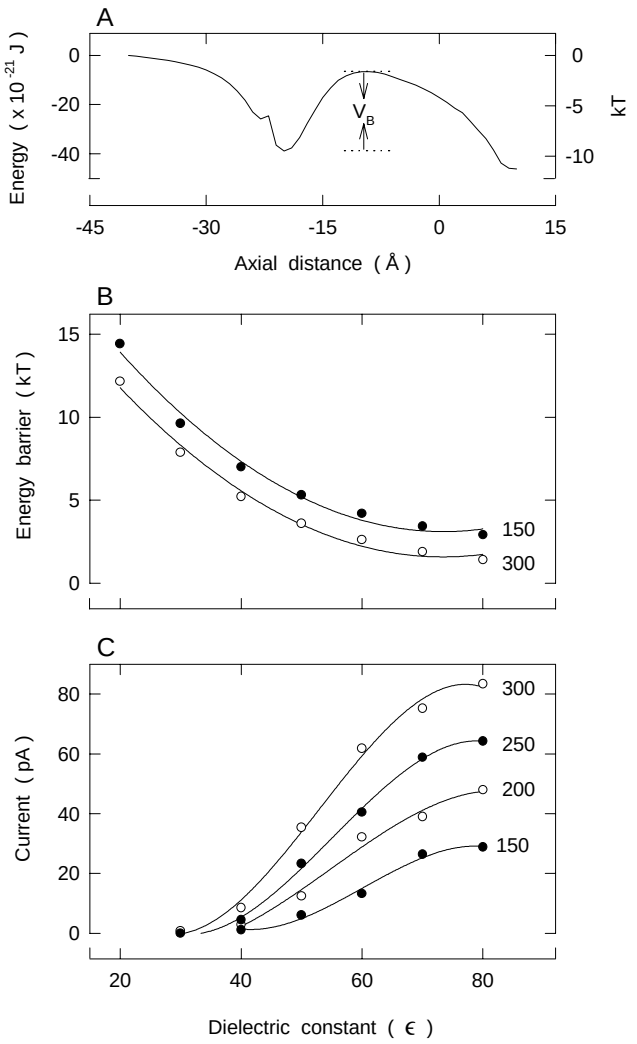

Figure 8.5: Effects of the effective dielectric constant on conductance. (A) A energy well near the channel entrance created by four mouth dipoles is encountered by an ion given that there are two resident ions in the selectivity filter. The energy minimization is carried out with $\epsilon = 30$ and an applied potential of 300 mV. An ion upon entering the well must surmount a barrier of height V_B to traverse the channel. (B) The height of the barrier V_B is plotted against the effective dielectric constant for two different values of applied potential, 150 mV (filled circles) and 300 mV (open circles). (C) The inward currents under the driving force of 300 mV (open circles), 250 mV (filled circles), 200 mV (open circles) and 150 mV (filled circles) are plotted against the effective dielectric constant. Each point is derived from a simulation period of either 1 μs (150, 200 and 250 mV) or 2 μs (300 mV).

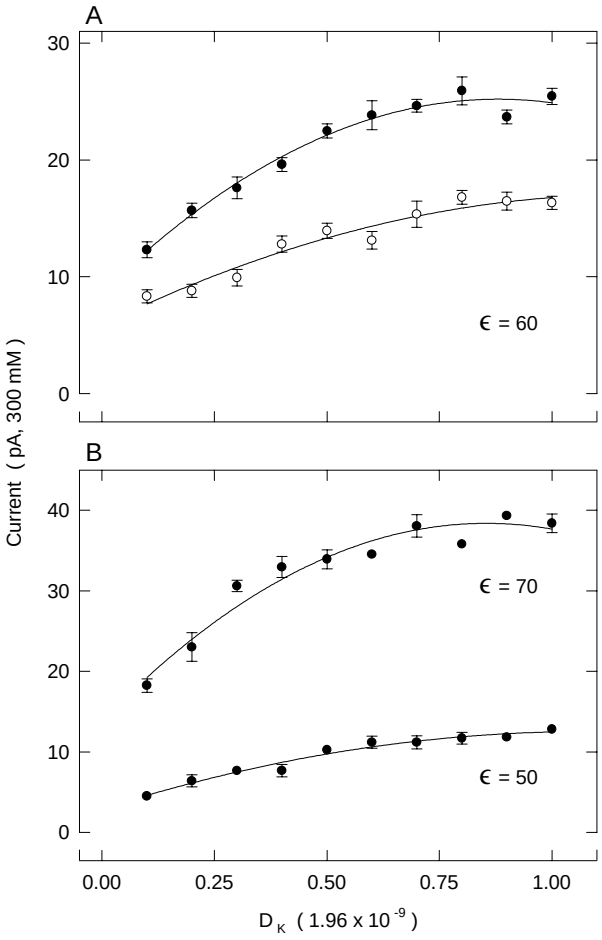

Figure 8.6: Effects of the diffusion coefficient on conductance. The diffusion coefficient of potassium ions in the selectivity filter, extending from $z = 7.5$ to 25 Å, is progressively lowered from the bulk value of 1.96×10^{-9} m^2/s and its effect on conductance is examined. (A) The outward (filled circles) and inward (open circles) current is plotted against diffusion coefficient in the selectivity filter, with $\epsilon = 60$ and an applied potential of 200 mV. (B) The outward current is plotted against diffusion coefficient in the selectivity filter for $\epsilon = 70$ (upper curve) and 50 (lower curve). Each point in (A) and (B) is derived from a simulation period of 1 μs.

(B). The filled and open circles in (A) represent, respectively, the outward and inward currents. The applied potential across the channel and the ionic concentration in the reservoir are kept constant at 200 mV and 300 mM, respectively. In contrast to bulk conductance, where current is proportional to the diffusion coefficient, the current in the potassium channel depends on D_{K} in a non-linear fashion. It decreases with decreasing D_{K} at a very slow rate at first (until D_{K} is reduced about 0.5 of its bulk value), and then becomes more or less proportional to D_{K}. When D_{K} is reduced to 1/3 of the bulk value, the current is only suppressed by about 30%.

8.3.4 Current-Voltage Relationships

The current-voltage relationships, shown in Fig. 8.7, are obtained with symmetrical solutions of 300 mM in both reservoirs. The diffusion coefficient in the selectivity filter is assumed to be the same as that in bulk electrolytes. Because the effective dielectric constant ϵ of the channel is unknown, we have determined the current-voltage curves, assuming ϵ to be 60, 70 and 80. The curves derived from these three conditions all reveal several distinct features. First, at any given applied potential, the outward current is larger than the inward current. Secondly, the magnitude of current across the channel at any given driving force increases steadily with increasing dielectric constant. The outward current at 100 mV is 6.7 ± 1.2, 11.8 ± 2.1 and 15.0 ± 1.0 pA when ϵ is assumed to be 60, 70 and 80, respectively (Fig. 8.7 A, B, & C). Because the current begins to saturate with increasing ionic concentrations (see later), the conductance at 150 mM K^+ will be slightly larger than 33, 59 and 75 pS at these three values of dielectric constants. Thirdly, the relationship is approximately linear when the applied potential is less than 100 mV, but it deviates systematically from Ohm's law with a further increase in the membrane potential. Given the results described in chapter 7 (see Fig. 7.8) and the preceding section (see Fig. 8.5), it seems reasonable to assume that this nonlinearity results from the presence of an energy barrier in the model channel.

To provide the solid lines in Fig. 8.7 we use a modification of the Pöschl-Teller function described in section 7.2.1:

$$I = \frac{\gamma V}{1 + \beta/[\exp(eV/V_{B1}) + \exp(-eV/V_{B2})]}, \tag{8.6}$$

where γ is the limiting conductance at large V, β is a dimensionless parameter and V_{B1} and V_{B2} are the right and left barrier heights. This function reduces to Ohm's law at very small and very large voltages, with conductance $\gamma/(1 + \beta/2)$ when the voltage is close to zero, and conductance γ when the voltage is positive and much greater than V_{B1} or negative and much smaller than V_{B2}. The solid lines are intended only to help visualize the conductance data, not to provide a physical interpretation, and for this reason the fit parameters are not given.

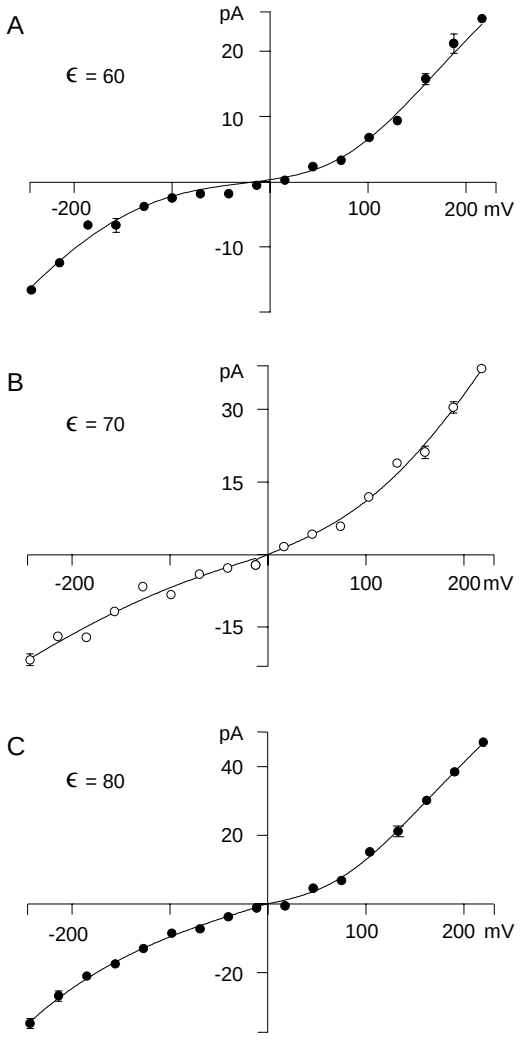

Figure 8.7: The current-voltage relationships. The current measured at various applied potentials is obtained with symmetrical solutions of 300 mM in both reservoirs. The solid lines fitted through data points are calculated from Eq. (8.6). The values of ϵ used for (A), (B) and (C) are 60, 70 and 80, respectively.

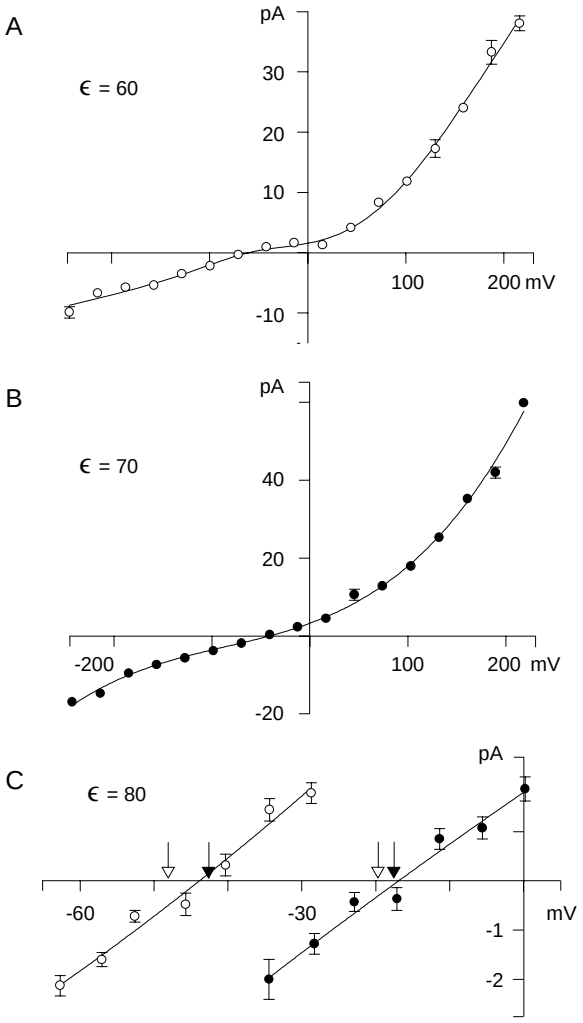

Figure 8.8: The current-voltage relationships. The current measured at various applied potentials is obtained with asymmetric solutions for $\epsilon = 60$ (A) and 70 (B). The concentration in the reservoir representing the intracellular space is 500 mM, whereas that representing the extracellular space is 100 mM. The solid lines drawn through the data are calculated with Eq. (8.6) multiplied by the Goldman factor, Eq. (8.7). For (C), obtained with $\epsilon = 80$, the measured concentrations in the intracellular and extracellular reservoirs are 482.0 mM and 71.5 mM (open circles) and 385.3 mM and 176.2 mM (filled circles). The open downward arrows indicate the reversal potential calculated from the Nernst equation. The predicted Nernst potentials taking the activity coefficients into account are indicated with filled downward arrows. The values of activity coefficients used for 71.5, 176.2, 386.3 and 482.0 mM are, respectively, 0.79, 0.73, 0.67 and 0.63.

The current-voltage relationships obtained with asymmetrical ionic solutions in the two reservoirs are shown in Fig. 8.8. The curves exhibited in the figure are obtained by assuming that ϵ in the channel is, respectively, 60 (A) and 70 (B). The ionic concentrations inside and outside are 500 mM and 100 mM. As expected, the asymmetry between the inward and outward currents is accentuated. As with the symmetrical solutions, an increase of ϵ from 60 to 70 causes an increase in the magnitude of currents flowing across the channel. The zero current of the two current-voltage relationships appears to be somewhere between -25 mV and -50 mV.

The solid lines fitted through the data points are obtained from Eq. (8.6) multiplied by a factor of the form:

$$\left[\frac{5-\exp(-eV/kT)}{1-\exp(-eV/kT)}\right]. \tag{8.7}$$

This factor comes from the Goldman-Hodgkin-Katz (GHK) equation which is usually used to fit the current-voltage curves of ion channels (see chapter 13 of Hille[31]). In the situation under discussion it is possible to express the GHK equation in the form:

$$I = KV\frac{1-5\exp(-eV/kT)}{1-\exp(-eV/kT)}, \tag{8.8}$$

where K is a constant and the factor of 5 arises from the outside to inside ratio of concentrations [18]. The GHK equation is derived under assumptions of a constant electric field and independent ion motion, which certainly do not apply to the model channel: as with the symmetric current-voltage results, the solid lines are only intended to help visualize the data.

To ascertain how closely the measured reversal potentials match with those predicted by the Nernst equation, we estimate currents flowing across the channel with two different ionic concentrations in the reservoirs and under various applied potentials. The concentrations of K^+ in the extracellular and intracellular aspects of the channel are computed from the average number of ions in the reservoirs throughout the simulation periods. The measured ionic concentrations in the left and right reservoirs in one series of simulations are 71.5 and 482.0 mM and in another series of simulations are 176.2 and 385.3 mM. Figure 8.8 shows the currents flowing across the channel at various applied potentials. Because the net current for these driving forces is small, the total simulation period of 3 μs is used to derive each data point. For the same reason, we use $\epsilon = 80$ for the effective dielectric constant of the channel, which results in a larger current flow. The reversal potential for each asymmetrical solutions is estimated by fitting a polynomial curve through the data points (solid line in Fig. 8.8 C). There are small but consistent discrepancies between the reversal potentials deduced from simulations and those predicted from the Nernst equation (indicated with open downward arrows). The zero currents occur at -45 mV and -17 mV when the

concentration ratios in the two reservoirs are, respectively, 6.7:1 and 2.2:1. The predicted reversal potentials are −48.1 mV and −19.7 mV. These discrepancies between the predicted and measured zero currents disappear if we take the activity coefficients of KCl at the measured ionic concentrations into account [73], as indicated by the filled arrows in Fig. 8.8 C. From a number of *I-V* curves obtained with asymmetrical solutions, we conclude that the zero current occurs at a potential predicted by the Nernst equation within the errors of simulations.

8.3.5 Ions in the channel

It is of interest to note where in the channel ions dwell predominantly. To compute the average number of ions inside the channel, we divide the channel into 32 thin sections and compute the time averages of potassium ions in each section. When a potential of 200 mV is applied so as to produce an outward current, two ions on average tend to reside in the channel. The preferred positions where ions dwell are in the selectivity filter at $z = 9.4$, 14.1 and 23.4 Å, as shown in Fig. 8.9 A. We note here that, although the histogram (Fig. 8.9 A) shows three distinct peaks near the selectivity filter, there are on average 1.5 ions in this region, as can be deduced by summing the heights of the bars. A similar sum for the peak near the intracellular entrance gives 0.5 ions, that is, an ion is present there 50% of the time. The preferential positions of the ions in the channel are shifted when the direction of the current is reversed by making inside negative with respect to outside. Under this condition, two ions mainly linger around $z = 9.4$ and 17.2 Å (Fig. 8.9 B). Thus, the preferred locations of ions in the channel depend on, among other factors, the direction and the strength of the applied field.

To better illustrate the behavior of ions under the influence of the electric and stochastic forces, we bisect the channel and denote the number of ions on the left and right hand sides by $[n_l, n_r]$. The occupation probabilities of distinct states are tabulated in Table 8.1 for five different potentials. At the bottom of the table, we give the average number of ions resident in the channel, which is about 2 regardless of the applied potential.

When the applied potential is 100 mV, which is relevant for the operation of the potassium channel, the most common occupation pattern is [0, 2]. That is, no ion is present in the first half (intracellular side) of the channel, while 2 ions are present in the second half (extracellular side). In addition to the patterns listed in Table 8.1, there are five other distinct patterns that are observed during the total simulation period of 0.5 μs (or 5 million time steps), but the frequencies of their occurrences are less than 1%. About 32,000 transitions occur between these patterns when the snapshot of the channel configuration is taken once every pico-second. The most common transitions are between [0, 2] and [0, 1], and between [1, 2] and [1, 1], which corresponds to the following process: driven by thermal energies, one of the

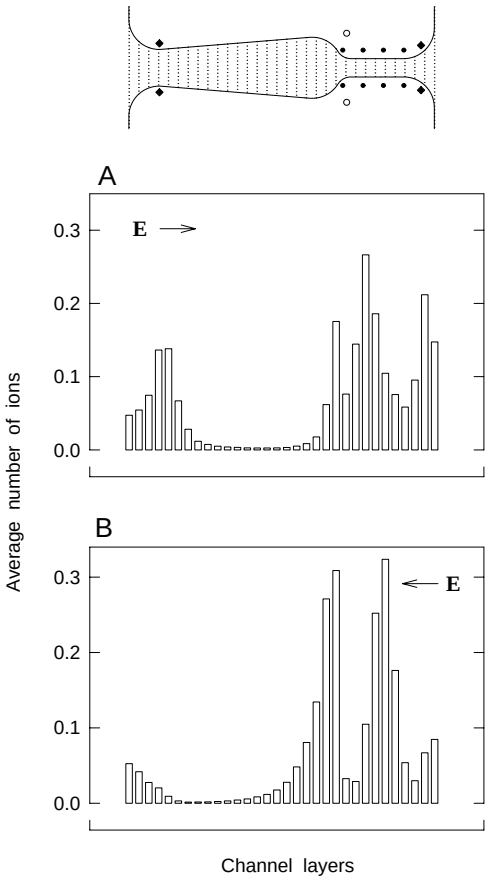

Figure 8.9: Concentrations of potassium ions in the channel. The channel is divided into 32 sections, as indicated in the inset, and the probability of ions present in each section over a simulation period of 0.5 μs is tabulated (bars). The ionic concentration in the reservoirs is 300 mM. The applied electric field in (A) is 2×10^7 V/m such that inside (left-hand side) is about 200 mV positive with respect to outside (right-hand side). The direction of the field is reversed to obtain the distribution shown in (B).

Table 8.1: Occupation probabilities of multi-ion states $[n_l, n_r]$ and the average number of ions in the channel $\langle n_l + n_r \rangle$ for different applied potentials.

$[n_l, n_r]$	-200 mv	-100 mV	100 mV	200 mV	300 mV
[0, 1]	3.5	3.4	12.1	15.2	17.2
[1, 1]	6.6	3.3	19.2	36.6	41.9
[0, 2]	78.9	78.2	49.2	30.3	25.3
[1, 2]	6.8	12.5	18.4	17.2	14.8
[0, 3]	3.8	2.4	-	-	-
Total %	99.6	99.8	98.9	99.3	99.2
$\langle n_l + n_r \rangle$	2.07	2.11	2.06	2.02	1.98

two ions in the second half of the channel escapes and then re-enters. The forward and backward transitions between these two sets account 64% of the total transitions. Less frequent transitions, occurring about 20% of all transitions, are between [0, 2] and [1, 2]. Finally, transitions between [0, 1] and [1, 1] account for 6% of the total transitions, while the forward transition between [1, 1] to [0, 2] accounts only for 0.3% of the total transitions.

8.3.6 Conductance-Concentration Relationships

If the transport of ions across the channel is determined by two independent processes, one of which depends on ionic concentration in the reservoir and one of which does not, then we expect that the current I will first increase with an increasing ionic concentration $[c]$ and then saturate, leading to a current-concentration relationship of the Michaelis-Menten form:

$$I = \frac{I_{\max}}{1 + K_s/[c]}, \tag{8.9}$$

so that the current approaches the saturation current $I_{\max}$ when $[c] \gg K_s$.

The magnitude of current across the channel plotted against the concentrations of potassium ions in the reservoirs, shown in Fig. 8.10, has the same shape as those observed experimentally [19, 59]. The two curves in (A) and (B) are the outward (filled circles) and inward (open circles) currents determined by assuming $\epsilon = 60$ (A) and $\epsilon = 70$ (B). The applied potentials used for (A) and (B) are, respectively, 200 mV and 150 mV. The conductance increases rapidly with an increasing ionic concentration at first and then saturates with a further increase in concentrations. The values of $I_{\max}$ and K_s

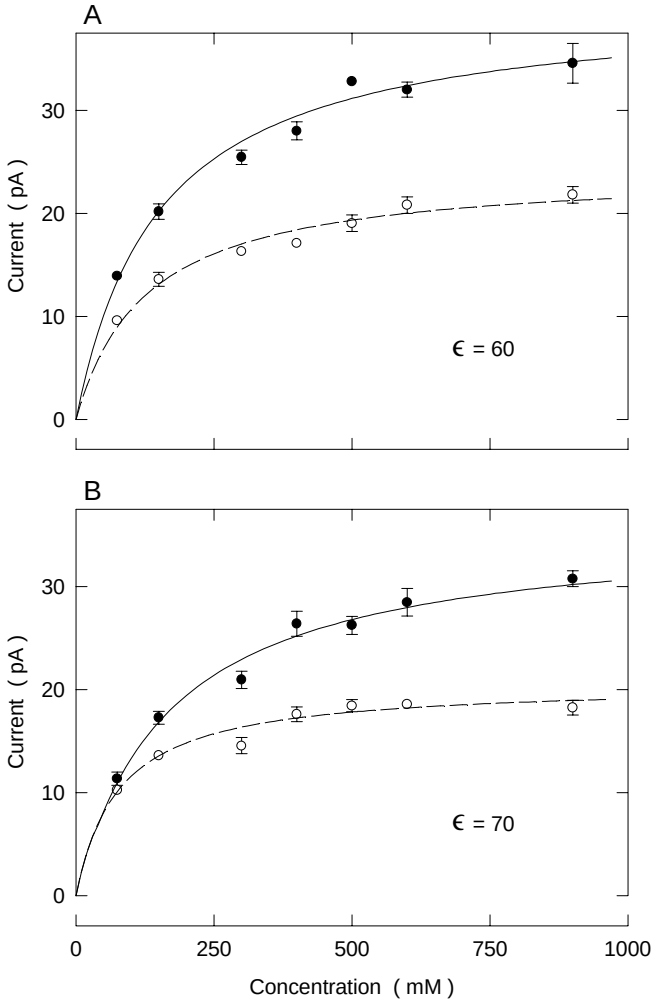

Figure 8.10: The conductance-concentration curves. The outward (filled circles) and inward (open circles) are obtained with symmetric solutions of varying concentrations in the two reservoirs. An applied potential of 200 mV and $\epsilon = 60$ are used for (A), while a potential of 150 mV and $\epsilon = 70$ are used for (B). The lines fitted through data points are calculated with Eq. (8.9).

used to fit the data points are: for A, 41 ± 1 pA and 151 ± 11 mM (outward currents), 24.2 ± 0.8 pA and 127 ± 11 mM; for B, 36 ± 1 pA and 169 ± 15 mM (outward currents) and 20.6 ± 0.5 pA and 77 ± 9 mM. The concentrations for half-maximal currents K_s we derive are slightly higher than the experimentally determined value for a potassium channel from sarcoplasmic reticulum by Coronado et al. [19].

8.4 Discussion

The fixed charges in the model, as adjusted to give maximum conductance, are somewhat smaller than expected. The helix dipoles have charges of 0.6×10^{-19} C (giving a dipole moment of 96×10^{-19} Cm over a length of 16 Å), compared to a value of 0.8×10^{-19} C (or 12×10^{-19} Cm per 1.5 Å) calculated from the structure of an alpha helix [32]. The mouth dipoles also have charges of 0.6×10^{-19} C, where 1.6×10^{-19} C (one elementary charge) might be expected. However, it is possible that in a ring of negative charges like this some of the side chains would become protonated and lose their negative charge [3]. If only two of the side chains were charged this would be consistent with four mouth dipole charges of 0.8×10^{-19} C, although two charges of 1.6×10^{-19} C would be a better representation. The carbonyl dipole charges of 0.6×10^{-19} C are as expected for a carbonyl group [11], but considering the crudeness of the filter model and the doubts about the electrostatic calculations in this region, this must be considered fortuitous.

The adjusted dielectric constant of 60 for the water in the channel is not in agreement with molecular dynamics studies. The dielectric constant must be at least 60 for the model channel's conductance to agree with experiment. When the dielectric constant is reduced to 40 the model channel effectively ceases to conduct, at least for realistic voltages. Molecular dynamics studies of water in spherical cavities [74] and narrow pores [66] suggest that the dielectric constant in confined spaces is substantially reduced compared to the bulk value.

Given the high dielectric constant the conductance characteristics of the model channel are reasonable, but they have not been compared in detail to the characteristics of real KcsA channels, as the comprehensive electrophysiological data required to do so is not yet available. The overall conductance of the model channel of around 33 pS (at 150 mM potassium and for $\epsilon = 60$) is in reasonable agreement with the experimental single channel conductance of around 40 pS (at 200 mM potassium) for the most common conductance state [67]. The model channel's conductance saturates in a manner similar to real potassium channels, showing the expected Michaelis-Menten form. The partial rectification shown by the model channel for symmetric solutions is interesting, as it is probably a multi-ion effect, but it is difficult to compare with results from real channels. Most potassium channels rectify,

but they do so by gating or ionic block, meaning that usually only one half of the current-voltage curve is available.

The x-ray crystallography done on the KcsA channel [21] shows three preferred ion positions: two in the selectivity filter and one in the central cavity. As described below, the model channel seems to have stable states in which the ions preferentially occupy particular positions depending on the applied voltage and the number of ions in the channel. If so this is consistent with the presence of sharply defined ion positions. The model channel contains an average of around two ions, but this is not in itself inconsistent with a channel with three ion positions, since the positions need not be occupied all the time. Nor is it inconsistent with ionic flux coupling results which suggest more than two ions in a conducting potassium channel [31], since the model channel may be more likely to conduct when it contains three ions, and almost certainly does not conduct when it contains one. Averages need to be interpreted with care; the real story is in the distribution and this is where a discrepancy shows up. In the model channel ions are concentrated in three areas, the selectivity filter, the cytoplasmic mouth, and the extracellular mouth, but never in the central cavity. This is a clear difference between the model channel and experimental results.

The likely causes of this discrepancy and the requirement for a high dielectric constant are inaccuracies in estimation of the electrostatic forces and problems with charge positions in the model channel. It is possible that the whole concept of modelling this channel with diffusion and electrostatics is wrong, and binding sites and hopping really are essential to its operation. This seems to us unlikely, however, since the model channel does show many similarities with the real channel, and multi-ion channels in general. Also the main problem, the lack of ion concentration in the central cavity, is in a region expected to be controlled by electrostatics and diffusion. Possible improvements to the electrostatics techniques are described in section 3.1.4, and these may be needed to provide an accurate description of the channel. Surprisingly the crude selectivity filter model works reasonably well, concentrating ions but allowing conductance by mutual destabilization. However, it may be that the small dipoles in the filter (which have some ability to move in the real channel) need to be represented in part by a locally increased dielectric constant rather than fixed charges. This could lead to a reduction of their long range effect in the central cavity without removing their ability to concentrate ions in the selectivity filter. Another possibility is that the arbitrarily placed counter charges in the mouth dipoles are too close to the negative charges surrounding the mouths of the channel. This could result in artificially sharp energy wells, leading to the barrier near the cytoplasmic mouth which seems to cause of the need for a large dielectric constant. A good start towards a better model channel would be to generate the shape and charge positions directly from the molecular structure, rather than in the rather ad-hoc way described above. This would also have the

advantage of reducing the number of adjustable parameters.

It seems we have constructed a working model of a multi-ion channel, albeit with an unrealistically high dielectric constant, but not a functional replica of the KcsA channel. After optimization of dipole strengths and the dielectric constant the model channel has a conductance comparable with the KcsA channel and other potassium channels. The concentration profiles (Fig. 8.9) and occupation probabilities (Table 8.1) show that the channel is usually occupied by two ions, and almost always by at least one, and this suggests that the channel contains at least two ions while conducting, since a single ion traversing the channel would leave it unoccupied when it exited. The current through the model channel saturates with increasing concentration (Fig. 8.10), as is characteristic of multi-ion channels. The channel also shows partial rectification with symmetrical solutions (Fig. 8.7), and it seems likely that this is an effect of the interactions between multiple ions within the channel.

So the model channel is multi-ion, and it shows conductance characteristics similar to real multi-ion channels. Its operation cannot, however, be explained in terms of hopping between binding sites as is usual for multi-ion channels. The model channel contains no binding sites, only a broad energy well (Fig 8.2 A), and all transport is by simulated diffusion. If an explanation of its conductance is desired, a different mechanism must be found. The existence of such a mechanism is useful because, if understood, it might lead to an alternative theory to RRT for conductance in multi-ion channels. Although RRT is the best available theory for summarizing experimental conductance data from a channel, and provides intuitive explanations for aspects of the the conductance of multi-ion channels that other theories cannot, the physical basis for its application to channels is doubtful (see section 2.1).

The concentration profile for an outward electric field (Fig. 8.9 A) shows that ions spend most of their time in particular regions of the model channel. Ions are concentrated in the selectivity filter and the cytoplasmic and extracellular mouth regions: they are rarely found in the inner pore or central cavity. Since ions must travel through the inner pore for the channel to conduct (which it does), the low concentration in this region suggests that the ions move through rapidly, and that transitions are relatively infrequent compared to the time spent in the channel mouths and selectivity filter. The concentration of ions in particular locations in the model channel (as evidenced by peaks in the concentration profiles) is consistent with the idea of binding sites. However, the single ion energy profile (Fig. 8.2 A, curve d) is smooth, showing only a broad energy well centred on the selectivity filter, and a very shallow well near the cytoplasmic mouth. There is no sign of the sharp localized wells that would indicate binding sites. This is not surprising given the method used to calculate the electrostatic potential (macroscopic electrostatics). The real channel may or may not contain ion binding sites,

but the concentration profiles are for the model channel and so the peaks in them cannot be explained in this way. A likely explanation is that the broad energy well attracts more that one ion to the channel, these ions change the energy profile experienced by each other (as they must), and that the interactions between the ions and the channel create temporary energy wells which confine the ions and cause the peaks. In other words the ions self-organize into particular positions in the channel depending on the number of ions present and the strength and direction of the applied field.

The multi-ion energy profiles (Figs. 8.2 and 8.5) support this interpretation. In Fig. 8.2 B energy profiles are calculated while another ion is fixed in the selectivity filter. The energy wells are sharper then that of the single ion profile (Fig. 8.2 A, curve d), and are consistent with two ions residing in particular locations at either end of the selectivity filter, and producing two separate peaks in the concentration profile. In Fig 8.2 C the energy profile is calculated for an ion entering the channel from the cytoplasmic end with two other ions already in the selectivity filter. These two ions have their positions altered to minimize energy as the first ion is moved into the channel (see section 8.2.1). The energy profile shows a well near the cytoplasmic mouth and a barrier centred on the inner pore. This is consistent with the peak in the concentration profile (Fig 8.9 A) just inside the cytoplasmic mouth, and the low concentrations in the inner pore. The height of the barrier in the multi-ion profile depends on the dielectric constant used for the simulation (Fig. 8.5 B): as the dielectric constant is increased, the inner pore and central cavity become more effective at hydrating the ion (as simulated by macroscopic electrostatics), and the barrier is reduced. This in turn increases the conductance of the channel (Fig. 8.5 C). Considering a single ion at at time does not provide such a direct explanation: as the dielectric constant increases, so does the depth of the well in the single ion profile, but it is not clear why this should cause the conductance of the channel to increase. The multi-ion energy profiles, based on the assumption of multiple ions self-organizing in the model channel, provide an explanation for the peaks in the concentration profiles, as well as the increase of conductance with increasing dielectric constant.

If the ions in the model channel self-organize into stable states, then transition between these states is probably by rapid diffusion, as indicated by the low concentration of ions in the inner pore. This suggests an overall picture of relatively stable states with rapid transitions between states. This is similar to RRT but with different physical causes. The occupation probabilities summarized in table 8.1 are a preliminary attempt to recognize possible states. Since the division between right and left halves of the channel is in the rarely occupied inner pore, an ion in the left half is probably in the well near the cytoplasmic mouth, while ions in the right half are probably in the selectivity filter or extracellular mouth. Unfortunately, while the occupation probabilities give some idea of possible states, they do

not give clear information about transitions between states. Some examples of transition probabilities are given in the text (section 8.3.5), but most of the transitions consist of ions briefly entering the mouth regions of the channel and immediately leaving. The problem is that the occupation probabilities do not represent identified stable states, but simply the very rough positions of the ions: each occupation pattern may represent zero or more stable states as well as various transient events. If there are stable states, then the patterns containing them will dominate the probabilities. Thus the distribution of probabilities in the table is some evidence that stable states exist in the model channel. Transitions between stable states are relatively rare, however, and cannot easily be picked out of the occupation probability data. Clearly a more sophisticated method of state identification and analysis is needed.

If ions in the model channel self-organize to form stable states this implies that the preferred positions of ions may change depending on the number of ions in the channel and the strength and direction of the electric field. There is evidence of this happening in the concentration profiles (Fig. 8.9) and the occupation probabilities (Table 8.1). The concentration profile for +200 mV (Fig. 8.9 A) shows a peak near the cytoplasmic mouth and one main peak in the centre of the selectivity filter, with subsidiary peaks on either side in the extracellular mouth and at the cytoplasmic end of the filter. In contrast the concentration profile for -200 mV (Fig. 8.9 B) shows two strong peaks in the selectivity filter, with not many ions elsewhere. This seems to correspond to the dominant [0, 2] pattern for occupancy under these conditions, which has about 80% probability. It is possible that this concentration profile represents a stable state which gives rise to the prominence of the [0, 2] pattern. The occupancy patterns for +200 mV have a more even spread of probabilities, indicating that the concentration profile may be an amalgam of several states. The patterns [1, 1] and [1, 2] make up over 50% of the probability, which could explain the peak near the cytoplasmic mouth. All four dominant patterns have ions in the right half of the channel: these ions may be in different places and this could explain the confusion of peaks in and near the selectivity filter.

In summary, this attempt to model the KcsA channel by Brownian dynamics simulation can only be regarded as a mixed success. The lack of ion concentration in the central cavity is a major deviation from experimental results, and the requirement for a large dielectric constant is probably wrong. However, the model channel has many similarities to the real channel. It has comparable conductance, and current through it saturates as in a real potassium channel. It also has sharp concentrations of ions in the selectivity filter similar to those in the KcsA channel. The values of the fixed charges, fitted to maximize conductance, are quite reasonable. These similarities suggest that the basic approach is sound, but that the model channel needs to be improved and made closer to the experimental structure, and that methods

of estimating the electrostatic forces need to be improved. Nevertheless, the effort has established that a model based on diffusion and electrostatics can produce a working multi-ion channel. In addition the way that the model channel seems to conduct by states and transitions may provide insight into conductance in multi-ion channels in general, and the reasons for the success of RRT in channels despite its dubious physical assumptions.

Chapter 9

Conclusion

The major technical challenge of this project was the production of fast, flexible, and accurate solutions to Poisson's equation. The iterative method is flexible but slow: it produces solutions for a wide variety of channel shapes, but can not produce these solutions quickly enough to allow useful BD simulations. The analytical method is faster and more accurate, but is limited to a toroidal channel boundary, and is still not quick enough for a BD simulation to predict conductance. The lookup table method gives access to the flexible solutions of the iterative method with sufficient speed to allow long BD simulations capable of predicting conductance. Although the analytical method might seem to be rendered obsolete, it is still very useful for checking the iterative and lookup table methods. The ability to compare solutions of Poisson's equation arrived at by completely different methods gives us a high level of confidence in the correct operation of our programs.

When used in Brownian dynamics simulations, these techniques for rapidly solving Poisson's equation produce quantitative predictions from model channels. The results from a single ion channel show that a narrow pore through a low dielectric medium presents a large energy barrier to permeating ions. Dipoles in the channel wall are needed to overcome this barrier, which is not removed by the presence of counter-ions free to diffuse. The results for a multi-ion channel show reasonable agreement with the conductance characteristics of real channels. They also suggest that multiple ions form states in the channel, with permeation occurring by transition between these states. Although complicated and computer intensive, our theory of conductance in ion channels is based on physical principles, and makes quantitative predictions from channel structure. In addition, the predictions made from an experimentally based channel model are at least similar to the expected values.

Despite this progress, there are many improvements that could be made to the theory, and much more work that should be done. An obvious need is for detailed comparison with experimental conductance results, to rigor-

ously test the theory. One difficulty here is finding good conductance data and structural data for the same channel. Now that the structure of the KcsA channel has been determined, this channel will likely become the subject of many experimental studies, so this is one good prospect. Another approach is structural modelling, attempting to match the experimental characteristics of a channel by guessing the structure. This requires a good understanding of how changes to the structure of the model affect its conductance, an understanding that we do not yet have. It also tends to rely on the accuracy of predictions from the theory, rather than verifying these predictions. Nevertheless, attempts at structural modelling may draw attention to weaknesses in our theory and techniques, and start to produce an intuitive understanding of the link between channel structure and conductance.

Improvements could be made to the iterative and lookup table methods, and the Brownian dynamics techniques. A new iterative algorithm based on a three dimensional grid would be desirable, as it would be able to accommodate changes in dielectric constant throughout the simulation in a self-consistent way. Some difficulties would be dealing with a smoothly curving dielectric boundary, and providing enough accuracy in the critical neck region of the channel. The lookup table algorithms need to be revised, to avoid the interpolation errors that can occur at the mouth of the channel, to improve the accuracy of interpolation for the 2d table, and perhaps to reduce the size of the tables to the extent that the algorithm is efficient on a RISC architecture machine. While the basic BD algorithm is a good one, able to cope with timesteps of any length, the algorithms describing the boundaries of the simulation are somewhat arbitrary. Better stochastic boundaries would allow the electro-chemical potentials of the reservoirs to be set, rather than estimated. Note that in Fig 8.8 the concentrations in the reservoirs have to measured from the simulations in order to correctly predict the reversal potential. The reflective boundaries and ion exclusion algorithms (section 5.3.2) are also undesirable. This problem could be solved by an adaptive timestep algorithm that varied the timestep from long to short depending on the proximity of ions to each other or the boundary. Such an algorithm would allow the reflective boundaries to be replaced by short range forces.

However, one of the ideas produced by the current algorithms shows great promise for future research, perhaps of more significance than making incremental improvements the existing theory. The observation that the model potassium channel may exhibit states and transition probabilities raises the prospect of providing reaction rate theory with a physical basis in channels, perhaps resulting in a simple theory of channel conductance with better explanatory power than a complex simulation. The first step would be to confirm the link between RRT and the potassium channel model, by doing an RRT analysis of the model's conductance, and comparing this to an improved state analysis of the movement of ions in the model channel.

Turning such a link into a useful theory would be harder, as diffusion over a barrier is theoretically much more complicated than hopping over a barrier. In kinetic hopping, energy is conserved, so the probability of crossing depends only on the barrier's height. Diffusion, however, is a dispersive process, and the shape and width of the barrier affect the probability of crossing. Nevertheless, this avenue should be pursued.

Bibliography

[1] M. Abramowitz and I. A. Stegun. *Handbook of Mathematical Functions*. Dover, New York, 1965.

[2] D. J. Adams, T. M. Dwyer, and B. Hille. The permeability of the endplate channel to monovalent and divalent metal cations. *Journal of General Physiology*, 75:493–510, 1980.

[3] C. Adcock, G. R. Smith, and M. S. P. Sansom. Electrostatics and ion selectivity of ligand-gated channels. *Biophysical Journal*, 75:1121–1222, 1998.

[4] M. P. Allen and D. J. Tildesley. *Computer Simulation of Liquids*. Clarendon Press, Oxford, 1987.

[5] T. W. Allen, S. Kuyucak, and S.-H. Chung. The effect of hydrophobic and hydrophilic channel walls on the structure and diffusion of water and ions. *Journal of Chemical Physics*, 111:7985–7999, 1999.

[6] T. W. Allen, S. Kuyucak, and S.-H. Chung. Molecular dynamics study of the KcsA potassium channel. *Biophysical Journal*, 77:2502–2516, 1999.

[7] P. W. Atkins. *Physical Chemistry*. Oxford University Press, Oxford, fifth edition, 1994.

[8] S. Bek and E. Jakobsson. Brownian dynamics study of a multiply-occupied cation channel: Application to understanding permeation in potassium channels. *Biophysical Journal*, 66:1028–1038, 1994.

[9] H. J. C. Berendsen, J. P. M. Postma, W. F. van Gunsteren, and J. Hermans. Interaction models for water in relation to protein hydration. In B. Pullman, editor, *Intermolecular Forces*, number 14 in Jerusalem Symposium on Quantum Chemistry and Biochemistry, pages 331–342. D. Reidel Publishing Company, Dordrecht, Holland, 1981.

[10] J. O'M. Bockris and A. K. N. Reddy. *Modern Electrochemistry*, volume 1. Plenum Press, New York, 1970.

[11] B. R. Brooks, R. E. Bruccoleri, B. D. Olafson, D. J. States, S. Swaminathan, and M. Karplus. CHARMM: a program for macromolecular energy, minimization and dynamic calculations. *Journal of Computational Chemistry*, 4:187–217, 1983.

[12] F. Buda, G. L. Chiarotti, R. Car, and M. Parrinello. Proton diffusion in silicon. *Physical Review Letters*, 63:294–297, 1989.

[13] R. Car and M. Parrinello. Unified approach for molecular dynamics and density-functional theory. *Physical Review Letters*, 55:2471–2474, 1985.

[14] D. Chen, J. Lear, and R. Eisenberg. Permeation through an open channel: Poisson-Nernst-Plank theory of a synthetic ion channel. *Biophysical Journal*, 72:97–116, 1997.

[15] D. Chen, Le Xu, A. Tripathy, G. Meissner, and B. Eisenberg. Permeation through the calcium release channel of cardiac muscle. *Biophysical Journal*, 73:1337–1354, 1997.

[16] D. Chen, Le Xu, A. Tripathy, G. Meissner, and B. Eisenberg. Selectivity and permeation through the calcium release channel of cardiac muscle: Alkali metal ions. *Biophysical Journal*, 76:1346–1366, 1999.

[17] S.-W Chiu, J. A. Novotny, and E. Jakobsson. The nature of ion and water barrier crossings in a simulated ion channel. *Biophysical Journal*, 64:98–108, 1993.

[18] S.-H. Chung, M. Hoyles, T. Allen, and S. Kuyucak. Study of ionic currents across a model membrane channel using Brownian dynamics. *Biophysical Journal*, 75:793–809, 1998.

[19] R. Coronado, R. L. Rosenberg, and C. Miller. Ionic selectivity, saturation, and block in a K^+-selective channel from sarcoplasmic reticulum. *Journal of General Physiology*, 76:425–446, 1980.

[20] J. A. Dani and D. G. Levitt. Diffusion and kinetic approaches to describe permeation in ionic channels. *Journal of Theoretical Biology*, 146:289–301, 1990.

[21] D. A. Doyle, J. M. Cabral, R. A. Pfuetzner, A. Kuo, J. M. Gulbis, S. L. Cohen, B. T. Chait, and R. MacKinnon. The structure of the potassium channel: Molecular basis of K^+ conduction and selectivity. *Science*, 280:69–73, 1998.

[22] T. M. Dwyer, D. J. Adams, and B. Hille. The permeability of the endplate channel to organic cations in frog muscle. *Journal of General Physiology*, 75:469–492, 1980.

[23] R. S. Eisenberg. Computing the field in proteins and channels. *The Journal of Membrane Biology*, 150:1–25, 1996.

[24] R. S. Eisenberg. From structure to function in open ionic channels. *The Journal of Membrane Biology*, 171:1–24, 1999.

[25] H. Eyring. The activated complex in chemical reactions. *Journal of Chemical Physics*, 3:107–115, 1935.

[26] H. Eyring. Viscosity, plasticity, and diffusion as examples of absolute reaction rates. *Journal of Chemical Physics*, 4:283–291, 1936.

[27] E. M. Fenwick, A. Marty, and E. Neher. A patch-clamp study of bovine chromaffin cells and of their sensitivity to acetylcholine. *Journal of Physiology*, 331:577–597, 1982.

[28] R. P. Feynman, R. B. Leighton, and M. Sands. *The Feynman Lectures on Physics*, volume II. Addison-Wesley Publishing Company, Reading, Massachusetts, 1964.

[29] J. Hermans, H. J. C. Berendsen, W. F. van Gunsteren, and J. P. M. Postma. A consistent empirical potential for water-protein interactions. *Biopolymers*, 23:1513–1518, 1984.

[30] T. L. Hill. *Statistical Mechanics*. McGraw-Hill, New York, 1956.

[31] B. Hille. *Ionic Channels of Excitable Membranes*. Sinauer Associates, Sunderland, Massachusetts, second edition, 1992.

[32] W. G. J. Hol, P. T. van Duijnen, and H. J. C. Berendsen. The α-helix dipole and the properties of proteins. *Nature*, 273:443–446, 1978.

[33] M. Hoyles, S. Kuyucak, and S.-H. Chung. Energy barrier presented to ions by the vestibule of the biological membrane channel. *Biophysical Journal*, 70:1628–1642, 1996.

[34] M. B. Jackson and H. Lecar. Single postsynaptic channel currents in tissue cultured muscle. *Nature*, 282:863–864, 1979.

[35] E. Jakobsson. Hierarchies of simulation methods in understanding biomolecular function. In *International Journal of Quantum Chemistry*, number 20 in Quantum Biology Symposium, pages 25–36. John Wiley & Sons, Inc., 1993.

[36] P. C. Jordan. Energy barriers for passage of ions through channels. Exact solution of two electrostatic problems. *Biophysical Chemistry*, 13:203–212, 1981.

[37] P. C. Jordan. Effect of pore structure on energy barriers and applied voltage profiles. I. Symmetrical channels. *Biophysical Journal*, 45:1091–1100, 1984.

[38] P. C. Jordan. Effect of pore structure on energy barriers and applied voltage profiles. II. Unsymmetrical channels. *Biophysical Journal*, 45:1101–1107, 1984.

[39] P. C. Jordan. Ion permeation and chemical kinetics. *Journal of General Physiology*, 114:601–603, 1999.

[40] M. Karplus. Molecular dynamics simulations in biology. *Nature*, 347:631–639, 1990.

[41] M. G. Kurnikova, R. D. Coalson, P. Graf, and A. Nitzan. A lattice relaxation algorithm for three-dimensional Poisson-Nernst-Plank theory with application to ion transport through the gramicidin A channel. *Biophysical Journal*, 76:652–656, 1999.

[42] S. Kuyucak, M. Hoyles, and S.-H. Chung. Analytical solutions of poisson's equation for realistic geometrical shapes of membrane ion channels. *Biophysical Journal*, 74:22–36, 1998.

[43] D. G. Levitt. Electrostatic calculations for an ion channel. I. Energy and potential profiles and interactions between ions. *Biophysical Journal*, 22:209–219, 1978.

[44] D. G. Levitt. Electrostatic calculations for an ion channel. II. Kinetic behavior of the gramicidin A channel. *Biophysical Journal*, 22:221–248, 1978.

[45] S. C. Li, M. Hoyles, S. Kuyucak, and S.-H. Chung. Brownian dynamics study of ion transport in the vestibule of membrane channels. *Biophysical Journal*, 74:37–47, 1998.

[46] J. D. Love. The dielectric ring in a uniform, axial, electrostatic field. *Journal of Mathematical Physics*, 13:1297–1304, 1972.

[47] R. M. Lynden-Bell and J. C. Rasaiah. Mobility and solvation of ions in channels. *Journal of Chemical Physics*, 105:9266–9280, 1996.

[48] D. Marx, M. Sprik, and M. Parrinello. Ab initio molecular dynamics of ion solvation: The case of Be^{2+} in water. *Chemical Physics Letters*, 273:360–366, 1997.

[49] R. J. Maurer. Deviations from ohm's law in soda lime glass. *Journal of Chemical Physics*, 9:579–584, 1941.

[50] L. M. Milne-Thompson. *The Calculus of Finite Differences*. Macmillan and Co., Ltd., London, 1960.

[51] L. A. Moran, K. G. Scrimgeour, H. R. Horton, R. S. Ochs, and J. D. Rawn. *Biochemistry*. Neil Patterson Publishers/Prentice-Hall, Inc., Englewood Cliffs, NJ, second edition, 1994.

[52] P. M. Morse and H. Feshbach. *Methods of Theoretical Physics*, volume II. McGraw-Hill, New York, 1953.

[53] W. Nonner, D. P. Chen, and B. Eisenberg. Progress and prospects in permeation. *Journal of General Physiology*, 113:773–782, 1999.

[54] W. Nonner and B. Eisenberg. Ion permeation and glutamate residues linked by Poisson-Nernst-Plank theory in l-type calcium channels. *Biophysical Journal*, 75:1287–1305, 1998.

[55] United States National Bureau of Standards Computation Laboratory. *Tables of Associated Legendre Functions*. Columbia University Press, New York, 1945.

[56] A. Parsegian. Energy of an ion crossing a low dielectric membrane: Solutions to four relevant electrostatic problems. *Nature*, 221:844–846, 1969.

[57] M. B. Partenskii and P. C. Jordan. Nonlinear dielectric behaviour of water in transmembrane ion channels: Ion energy barriers and the channel dielectric constant. *Journal of Physical Chemistry*, 96:3906–3910, 1992.

[58] W. H. Press, B. P. Flannery, S. A. Teukolsky, and W. T. Vetterling. *Numerical Recipes*. Cambridge University Press, New York, second edition, 1992.

[59] J. L. Rae, R. A. Levis, and R. S. Eisenberg. Ionic channels in ocular epithelia. In T. Narahashi, editor, *Ion Channels*, volume 1, pages 283–327. Plenum Press, New York, 1988.

[60] A. A. Rashin and B. Honig. Reevaluation of the born model of ion hydration. *Journal of Physical Chemistry*, 89:5588–5593, 1985.

[61] F. Reif. *Fundamentals of Statistical and Thermal Physics*. McGraw-Hill Kogakusha, Tokyo, 1965.

[62] D. K. Remler and P. A. Madden. Molecular dynamics without effective potentials via the Car-Parrinello approach. *Molecular Physics*, 70:921–966, 1990.

[63] R. A. Robinson and R. H. Stokes. *Electrolyte Solutions*. Butterworths Scientific Publications, London, 1959.

[64] B. Roux and M. Karplus. Ion transport in a model gramicidin channel: Structure and thermodynamics. *Biophysical Journal*, 59:961–981, 1991.

[65] M. S. P. Sansom, C. Adcock, and G. R. Smith. Modelling and simulation of ion channels: Applications to the nicotinic acetylcholine receptor. *Journal of Structural Biology*, 121:246–262, 1998.

[66] M. S. P. Sansom, G. R. Smith, C. Adcock, and P. C. Biggin. The dielectric properties of water within model transbilayer pores. *Biophysical Journal*, 73:2404–2415, 1997.

[67] H. Schrempf, O. Schmidt, R. Kümmerlen, S. Hinnah, D. Müller, M. Betzler, T. Steinkamp, and R. Wagner. A prokaryotic potassium ion channel with two predicted transmembrane segment from *Steptomyces lividans*. *The EMBO Journal*, 14:5170–5178, 1995.

[68] G. R. Smith and M. S. P. Sansom. Dynamic properties of Na^+ ions in models of ion channels: a molecular dynamics study. *Biophysical Journal*, 75:2767–2782, 1997.

[69] F. H. Stillinger and A. Rahman. Improved simulation of liquid water by molecular dynamics. *Journal of Chemical Physics*, 60:1545–1557, 1974.

[70] C. Toyoshima and N. Unwin. Ion channel of acetylcholine receptor reconstructed from images of postsynaptic membranes. *Nature*, 336:247–250, 1988.

[71] N. Unwin. The structure of ion channels in membranes of excitable cells. *Neuron*, 3:665–676, 1989.

[72] W. F. van Gunsteren and H. J. C. Berendsen. Algorithms for Brownian dynamics. *Molecular Physics*, 45:637–647, 1982.

[73] R. C. Weast, editor. *CRC Handbook of Chemistry and Physics*. CRC Press, Inc., Boca Ration, Florida, 1983.

[74] L. Zhang, H. T. Davis, D. M. Kroll, and H. S. White. Molecular dynamics simulations of water in a spherical cavity. *Journal of Physical Chemistry*, 99:2878–2884, 1995.